



Article

Intrinsic Defect Engineering in Eu^{3+} Doped ZnWO_4 for Annealing Temperature Tunable Photoluminescence

Bao-gai Zhai , Long Yang and Yuan Ming Huang *

School of Mathematics and Physics, Changzhou University, Changzhou 213164, Jiangsu, China; baogaizhai@126.com (B.-g.Z.); 15722741110@163.com (L.Y.)

* Correspondence: ymhuang@cczu.edu.cn; Tel./Fax: 86-519-86330301

Received: 5 December 2018; Accepted: 10 January 2019; Published: 15 January 2019



Abstract: Eu^{3+} doped ZnWO_4 phosphors were synthesized via the co-precipitation technique followed by subsequent thermal annealing in the range of 400–1000 °C. The phase, morphology, elemental composition, chemical states, optical absorption, and photoluminescence (PL) of the phosphors were characterized by X-ray diffraction, scanning electron microscopy, dispersive X-ray spectroscopy, X-ray photoelectron spectrometry, diffuse UV–vis reflectance spectroscopy, PL spectrophotometry, and PL lifetime spectroscopy, respectively. It is found that the PL from Eu^{3+} doped ZnWO_4 is tunable through the control of the annealing temperature. Density functional calculations and optical absorption confirm that thermal annealing created intrinsic defects in ZnWO_4 lattices play a pivotal role in the color tunable emissions of the Eu^{3+} doped ZnWO_4 phosphors. These data have demonstrated that intrinsic defect engineering in ZnWO_4 lattice is an alternative and effective strategy for tuning the emission color of Eu^{3+} doped ZnWO_4 . This work shows how to harness the intrinsic defects in ZnWO_4 for the preparation of color tunable light-emitting phosphors.

Keywords: ZnWO_4 ; defect engineering; photoluminescence; density functional calculation

1. Introduction

Zinc tungstate (ZnWO_4) is an important technological material having a diversity of applications in scintillators [1], photocatalysts [2], tunable laser host crystals [3], and light-emitting phosphors [4]. Among these applications, rare-earth doped ZnWO_4 phosphors have attracted intensive attentions due to the urgent demand of tunable light emitting phosphors for solid-state lighting [5–11]. As documented in the literature, the light-emitting properties of singly doped ZnWO_4 ($R = \text{Dy}^{3+}$ [5], Sm^{3+} [6], Eu^{3+} [7–13], Tb^{3+} [13]) and doubly doped ZnWO_4 ($R = \text{Eu}^{3+}$ and Dy^{3+} [14,15]) were investigated. Since the sharp emissions of trivalent rare-earth species are insensitive to external environment, variation in the dopant concentration of the rare-earth species has become the primarily choice to tune the emissions of rare-earth doped ZnWO_4 [5,8,13–15]. For example, Chen et al. tuned the color from blue through white to orange by adjusting the concentration of Eu^{3+} in ZnWO_4 nanorods [8]; Zhou et al. tuned the photoluminescence (PL) of Eu^{3+} and Dy^{3+} doubly ZnWO_4 by adjusting the doping concentrations of Eu^{3+} and Dy^{3+} in ZnWO_4 nanorods [14]. However, this strategy suffers from severe drawbacks and intrinsic limitations that cannot be solved by itself. One example of the drawback is the limited solubility of the rare-earth species in solids. For most of rare-earth oxides, their solubility in fluoride melts is less than 3 mol % [16]. For instance, Zhu et al. showed that the solubility of Nd_2O_3 and Nd_2O_3 in the molten salts of NdF_3 -LiF was in the range of 0.33–0.87 mol % [17]. Such a low solubility makes it difficult to vary the doping concentration in a wide range because segregation of the rare-earth ions occurs readily when the doping concentration exceeds their solubility. Another

example of the drawback is the concentration quenching in the PL intensity, which takes place when the doping concentration is higher than its critical concentration. For instance, Zhang et al. observed PL quenching when the concentration of Ce^{3+} ions in SrLu_2O_8 is larger than its critical concentration 0.2% [18]. Moreover, concentration quenching of PL was recorded in Eu^{3+} activated perovskites and Y_2MoO_6 [19,20], showing that the excess doping of rare earth ions usually decreased the emission intensity markedly. Therefore, it becomes necessary to develop an alternative but versatile strategy to tune the PL of rare-earth doped ZnWO_4 .

Intrinsic defect engineering in the crystal lattice of ZnWO_4 can provide an interesting solution to the problem on how to tune the emissions from rare-earth doped ZnWO_4 when the doping concentration is fixed. Previous work shows that intrinsic defects in undoped ZnWO_4 can give off intense blue emissions with their peak at about 480 nm [1,4,21], suggesting that the blue emissions can be readily modulated if the intrinsic defects in ZnWO_4 lattice can be controlled through an external condition. Thus, tunable PL from blue to red can be expected for Eu^{3+} doped ZnWO_4 if its blue emissions from intrinsic defect in ZnWO_4 host mix with the characteristic red emissions of Eu^{3+} dopant. In this work, we report color tunable PL from Eu-doped ZnWO_4 phosphors via annealing temperature controlled intrinsic defect engineering in ZnWO_4 lattice. Our results demonstrate that color tunable PL of Eu-doped ZnWO_4 phosphors can be achieved by simply tuning the annealing temperature in the range of 400–1000 °C. Rather than the control of rare-earth concentration in ZnWO_4 , this work shows how to harness the defect engineering in ZnWO_4 for color tunable emissions.

2. Experimental

Eu-doped ZnWO_4 precursors were prepared via the co-precipitation technique. The starting materials $\text{Zn}(\text{NO}_3)_2 \cdot 6\text{H}_2\text{O}$, $\text{Eu}(\text{NO}_3)_3 \cdot 6\text{H}_2\text{O}$, and $\text{Na}_2\text{WO}_4 \cdot 2\text{H}_2\text{O}$ were of analytical grade. At first, we prepared solution A by dissolving 0.04 mol of $\text{Zn}(\text{NO}_3)_2 \cdot 6\text{H}_2\text{O}$ and 0.002 mol of $\text{Eu}(\text{NO}_3)_3 \cdot 6\text{H}_2\text{O}$ in 100 mL deionized water, and solution B by dissolving 0.04 mol of $\text{Na}_2\text{WO}_4 \cdot 2\text{H}_2\text{O}$ in another 100 mL deionized water. Then white precipitates were formed when the two solutions were slowly mixed with each other. The pH value of the mixture was adjusted to 9 by the addition of appropriate amount of ammonia. The solids in the mixture were separated from the filtrate with a piece of filter paper. After having been washed with deionized water, the solids were dried in an oven at 60 °C for about 24 h. Finally, the dried precipitates were divided into four shares for subsequent annealing in air at 400, 600, 800, and 1000 °C, respectively. The time of annealing at each temperature was 2 h. The nominally doping concentration of Eu^{3+} species in each sample was 5 mol %.

Eu^{2+} doped ZnWO_4 standard was synthesized via self-propagating combustion method. 0.02 mole of zinc nitrate tetrahydrate, 0.0002 mole of europium nitrate hexahydrate and 0.6 mole of urea were dissolved into 50 mL deionized water to form a transparent solution. 0.02 mole of sodium tungstate dihydrate was dissolved in another 50 mL distilled water to form a transparent solution. White precipitates were formed when the two kinds of solutions were mixed. The mixture was transferred into a crucible for combustion in an air-filled furnace. The ignition temperature of the mixture was 800 °C. The large amount of reducing gases released in the process of combustion could reduce Eu^{3+} to Eu^{2+} . The nominally doping concentration of Eu^{2+} species in each sample was 1 mol %.

We employed an X-ray diffractometer (D/max 2500 PC, Rigaku Corporation, Akishima, Japan) to analyze the phase of the samples. The wavelength of the incident X-ray for the recorded X-ray diffraction (XRD) curves was 0.15405 nm. The morphology analysis of the phosphors was completed on the scanning electron microscope (SEM) (S-4800, Hitachi, Tokyo, Japan). The elemental composition in the phosphors was obtained by the energy dispersive X-ray (EDX) spectroscopic analysis. The X-ray photoelectron spectra (XPS) of the phosphors were recorded with the Escalab 250Xi spectrophotometer (Thermo Scientific, Waltham, MA, USA). Details on the measurements of the PL spectra, the diffused reflectance spectra and the PL lifetime spectra could be found elsewhere [22].

Using the density functional theory (DFT) module provided by Quantumwise (Atomistix ToolKit 11.8 package, Copenhagen, Denmark), we calculated the electronic structures of ZnWO_4 in the

framework of DFT. The exchange–correlation functional was described by the Perdew–Burke–Ernzerhof potential within the GGA+U scheme [23]. In our calculations, the lattice constants of ZnWO₄ were $a = 0.4691$ nm, $b = 0.572$ nm and $c = 0.4925$ nm while the angle $\beta = 90.64^\circ$. The experimental data on the lattice constants of ZnWO₄ single crystals are $a = 0.4691$ nm, $b = 0.5720$ nm, $c = 0.4925$ nm, and $\beta = 90.64^\circ$. Details on the density functional calculations can be found elsewhere [24].

3. Results and Discussion

3.1. XRD Analysis of Eu-Doped ZnWO₄

Figure 1 represents the XRD curves of Eu-doped ZnWO₄ precursors subjected to annealing at 400, 600, 800, and 1000 °C. In accordance with the standard XRD data for monoclinic ZnWO₄, the diffraction peaks at 15.36°, 18.68°, 23.68°, 24.32°, 31.10°, 37.98°, 49.90°, and 51.52° in Figure 1 can be assigned to the reflections from the (010), (100), (011), (110), (020), (200), (220), and (130) planes of monoclinic ZnWO₄, respectively [5,25]. The vertical bars in Figure 1 represent the XRD data of standard ZnWO₄ (JCPDS no. 15–0774) [5]. Obviously, the peak at 30.40° is ascribed to the combined contributions from (111) and (−111) crystallographic planes since the two diffractions are located too closely [2,5]. For the same reason, the peak located at 36.20° can be ascribed to the contributions from the pair of planes (021) and (002), whereas the peak located at 41.24° can be ascribed to the contributions from the pair of planes (121) and (−121). As a result, the diffraction peaks of the four annealed samples can be indexed to the monoclinic phase ZnWO₄, indicating the crystalline nature of Eu-doped ZnWO₄ solids. Additionally, XRD analysis shows that the Eu-doped ZnWO₄ precursors exhibit a broad band before annealing and when the annealing temperature is lower than 400 °C. The reason is that the diffraction (crystallized) domain is low enough to enlarge the peaks. Temperature is a significant variable in the crystallization of materials, it often influences nucleation and crystal growth of the material. In general, the molecules in amorphous metal oxides do not have sufficient time to arrange in the most stable positions, and they become frozen in positions other than those of a regular crystal. Consequently, a sufficiently high temperature can convert the internal structure of the solid from amorphous to crystalline, which accompanies a drastic mass transfer and usually results in increasing density.

Figure 2 depicts the unit cell of monoclinic ZnWO₄ (a) and the metal–oxygen octahedrons in monoclinic ZnWO₄ (b). As shown in Figure 2a, the unit cell of ZnWO₄ has two ZnWO₄ molecules, indicating that there are two Zn sites, two W sites and eight O sites in the unit cell of ZnWO₄. According to the data listed in JCPDS no. 15–0774 [5], the lattice parameters of standard ZnWO₄ are $a = 0.4691$ nm, $b = 0.5720$ nm, $c = 0.4925$ nm, and $\beta = 90.64^\circ$. In crystalline ZnWO₄, each W⁶⁺ ion is surrounded by six O ions to form a WO₆ octahedron, and each Zn²⁺ ion is coordinated with six O ions to form a ZnO₆ octahedron. The ZnO₆ and WO₆ octahedrons in ZnWO₄ are represented in Figure 2b. As shown in Figure 2b, ZnWO₄ consists of zig-zag ZnO₆ and WO₆ chains. For example, one zig-zag ZnO₆ chain is made up of edge-sharing ZnO₆ octahedrons, and one zig-zag WO₆ chain is made up of edge-sharing WO₆ octahedrons [26]. Moreover, each (ZnO₆–ZnO₆)_n chain is interlinked to four chains of (WO₆–WO₆)_n and vice versa. In the light of the crystal structures shown in Figure 2, we can understand why there is no lattice expansion upon Eu doping of ZnWO₄. Shannon gave a value of 74 pm for a 6-fold coordination which is observed in the Zn tungstate. However, the ionic radii mismatch between Zn and Eu does not give any change in the cell parameters probably due to the weak Eu doping amount [27]. Obviously, six coordinated W⁶⁺ sites ($r = 60$ pm) are too small for Eu³⁺ to occupy. Thus, the lattice expansion in Eu-doped ZnWO₄ grains can be neglected when the doping concentration of is 5 mol % only.

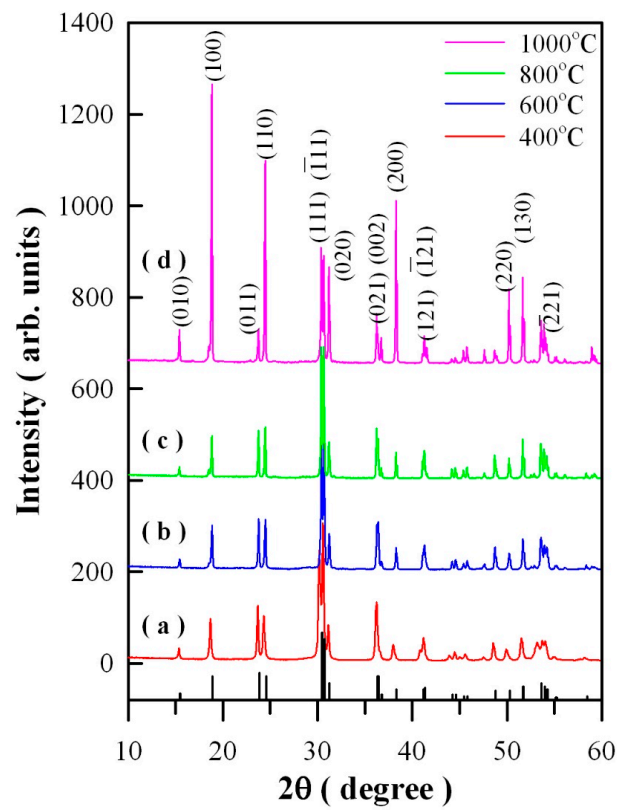


Figure 1. X-ray diffraction curves of Eu-doped ZnWO_4 precursors subjected to annealing at different temperatures: (a) 400 °C; (b) 600 °C; (c) 800 °C; and (d) 1000 °C. The standard diffraction data of monoclinic ZnWO_4 are shown at the bottom for comparison.

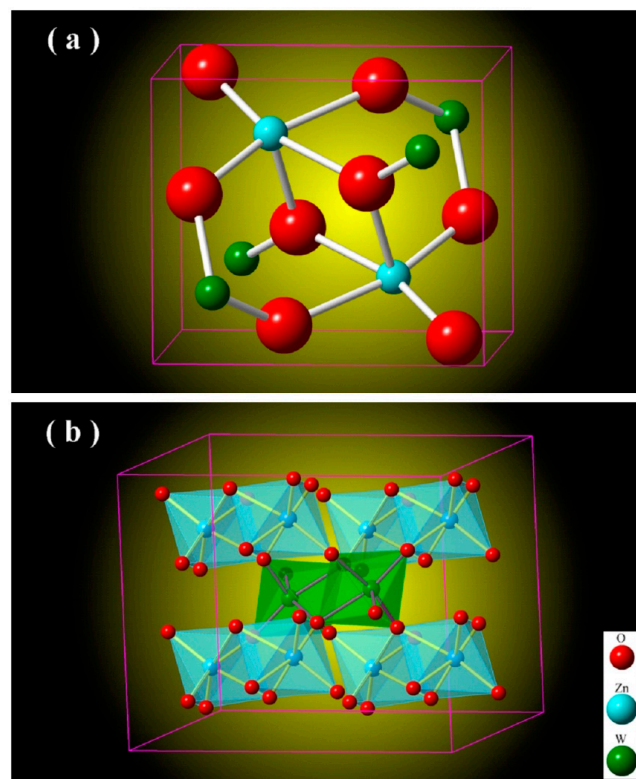


Figure 2. (a) Unit cell of monoclinic ZnWO_4 ; (b) Metal-oxygen octahedrons in monoclinic ZnWO_4 .

Figure 3 illustrates the Rietveld diffractograms of Eu-doped ZnWO_4 precursors subjected to annealing at different temperatures. The raw XRD data are represented by the open circles, and the calculated Rietveld diffractograms are represented by the solid green lines in Figure 3. [21,28]. It can be seen in Figure 3 that the calculated Rietveld diffractograms agree very well with the XRD curves a, b, and c but not for d. In XRD curve d, the diffraction intensities of the (100), (110), and (220) planes deviate significantly from those of calculated ones. The lattice parameters calculated from the Rietveld refinement are listed in Table 1. For the convenience of comparison, the lattice parameters of ZnWO_4 single crystals are listed in the last row in Table 1. For example, the calculated lattice parameters are $a = 0.4724$ nm, $b = 0.5725$ nm, $c = 0.4943$ nm, and $\beta = 90.9546^\circ$ for Eu-doped ZnWO_4 precursors subjected to annealing at 400°C . The calculated errors are ± 0.0003 nm for the lattice lengths and $\pm 0.0005^\circ$ for β .

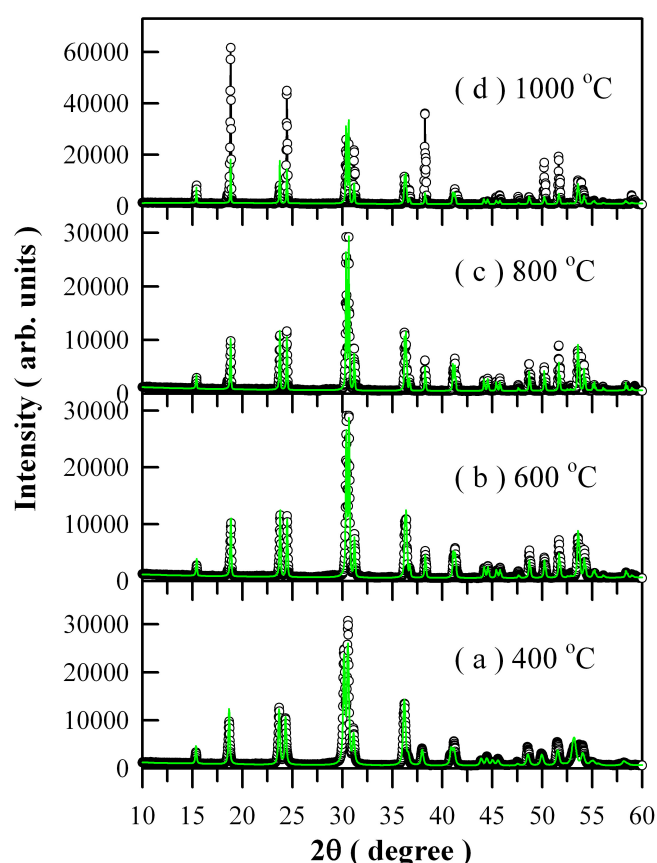


Figure 3. Rietveld analysis of the XRD curves of Eu-doped ZnWO_4 precursors subjected to annealing at different temperatures: (a) 400°C , (b) 600°C , (c) 800°C , and (d) 1000°C . Open circles: raw data. Solid green lines: Rietveld diffractograms.

Table 1. Lattice parameters of Eu-doped ZnWO_4 derived from whole spectrum fitting and Rietveld refinement. Lattice parameters of ZnWO_4 single crystals are listed in the last row for comparison.

T ($^\circ\text{C}$)	a (nm)	b (nm)	c (nm)	β ($^\circ$)
400	0.4724	0.5725	0.4943	90.9546
600	0.4693	0.5718	0.4927	90.6438
800	0.4692	0.5719	0.4927	90.6321
1000	0.4690	0.5718	0.4927	90.6191
Single crystal	0.4691	0.5720	0.4925	90.64

Figure 4 illustrates the differences between experimental and calculated XRD data of Eu-doped ZnWO_4 precursors subjected to annealing at different temperatures: (a) 400°C ; (b) 600°C ; (c) 800°C ;

and (d) 1000 °C. It can be seen in Figure 4 that good fit can be achieved for the three samples annealed at 400, 600, and 800 °C. However, it is surprising to observe a very bad fit for the 1000 °C annealed sample whereas the XRD data is correct. We are not sure what happens to the sample, and further investigation is required.

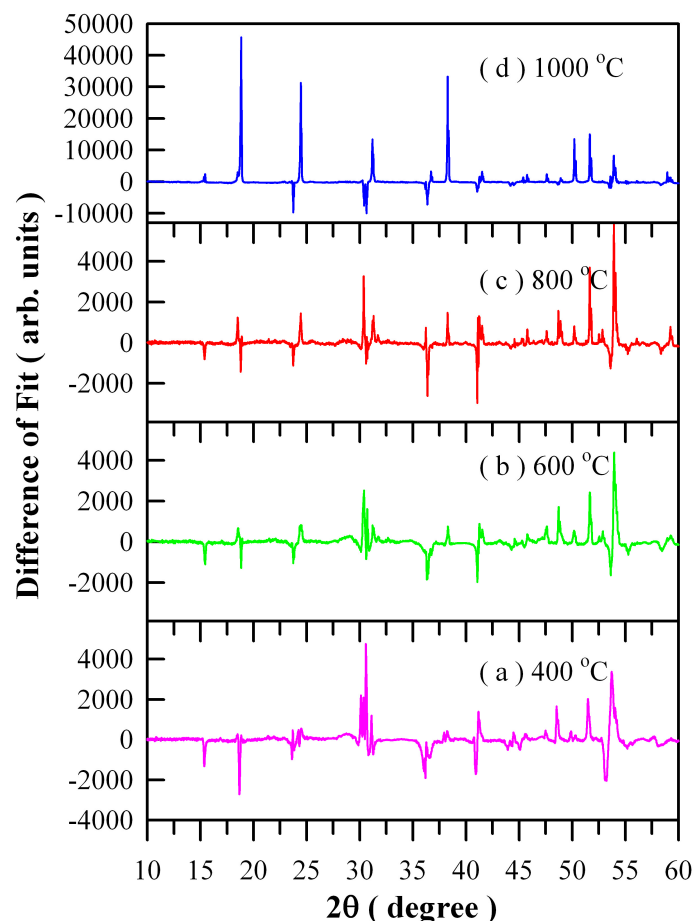


Figure 4. Differences between experimental and calculated XRD data of Eu-doped ZnWO₄ precursors subjected to annealing at different temperatures: (a) 400 °C; (b) 600 °C; (c) 800 °C; and (d) 1000 °C.

3.2. SEM Characterization of Eu-Doped ZnWO₄

Figure 5 shows the SEM micrographs of Eu-doped ZnWO₄ precursors subjected to annealing at 400, 600, 800, and 1000 °C. As shown in Figure 5a, the Eu-doped ZnWO₄ grains exhibit irregular shapes. According to crystal growth theory, the equilibrium shape of a crystal is determined by the Gibbs free energy, and the condition for minimization of the Gibbs free energy of a crystal formed at a constant volume is reduced to the minimization of surface energy. This is the Wulff's theorem. The equilibrium shape of a liquid droplet is evidently a sphere. The case of a crystal is more complicated as the latter is confined by crystal faces with different crystallographic orientations which have different specific surface energies. This means that the surface energy depends on the crystallographic orientations, and the formation of non-spherical ZnWO₄ grains is therefore thermodynamically favorable. Obviously, the average particle size of the ZnWO₄ grains is about 80 nm, the standard deviation of the particle size distribution is calculated to be 30 nm. In principle, these ZnWO₄ grains can grow bigger if the annealing temperature gets higher. Indeed, Figure 5b depicts that bigger Eu-doped ZnWO₄ grains are resulted as the thermal annealing temperature is raised to 600 °C. It can be seen in Figure 5b that the ZnWO₄ grains are irregular in shape with their particle sizes in the range of 80–800 nm. The average particle size of the ZnWO₄ grains is about 400 nm with the standard deviation of the particle size

distribution of about 190 nm. We can see that the Eu-doped ZnWO_4 grains are in the nanometer scale when the annealing temperature is 600 °C or less. Figure 5c shows that the micrometer sized ZnWO_4 grains are resulted when the annealing temperature is elevated to 800 °C. The particle size of ZnWO_4 grains ranges from 2 to 8 μm . The mean value of the particle sizes is about 4 μm with the standard deviation of the the distribution of 2 μm . Finally, these ZnWO_4 grains can continue their growth if the annealing temperature is increased further. Figure 5d shows that the lengths of ZnWO_4 grains are increased to about 20 μm when the annealing temperature is elevated to 1000 °C. In particular, these ZnWO_4 grains are rod-like with their aspect ratio ranging from 2 to 3. Overall, the micrographs in Figure 5 have demonstrated that the control of annealing temperature has significant impacts on both the particle size and the morphology of ZnWO_4 grains. The annealing temperature dependent particle size and morphology of Eu-doped ZnWO_4 can generate significant effects on their surface area and surface defects, which in turn lead to dramatic changes in the optical absorption and emissions of Eu-doped ZnWO_4 .

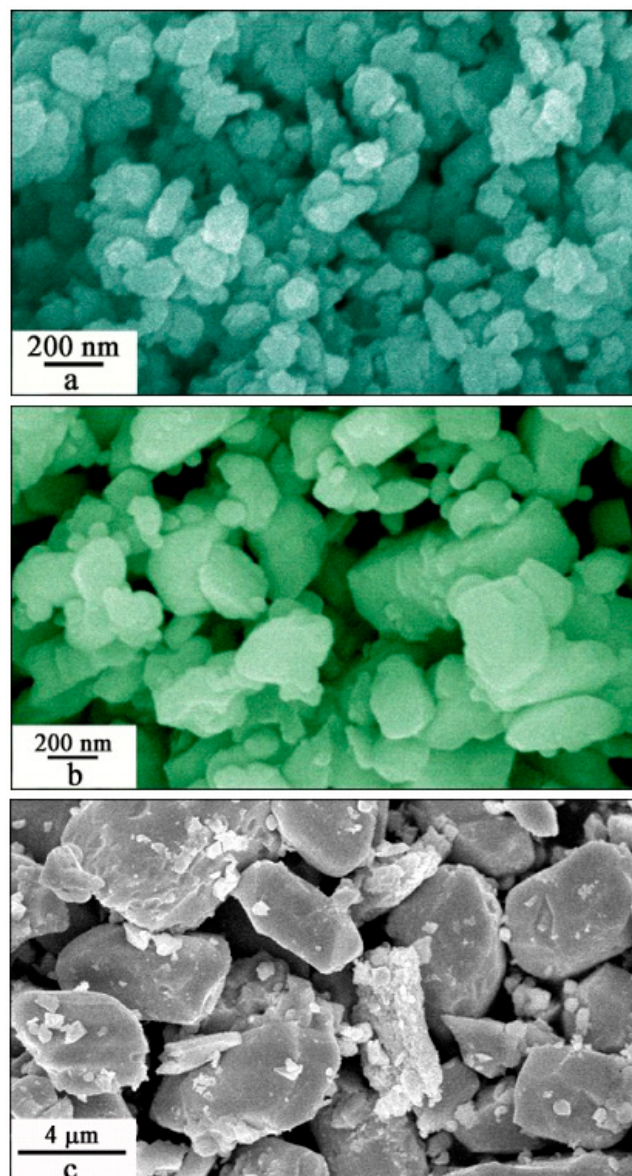


Figure 5. Cont.

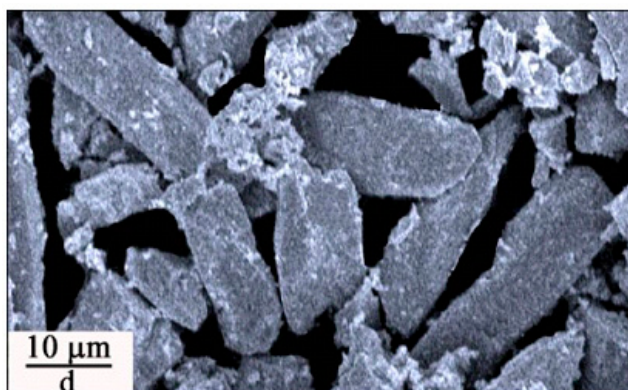


Figure 5. SEM micrographs of Eu-doped ZnWO₄ precursors subjected to annealing at different temperatures: (a) 400 °C; (b) 600 °C; (c) 800 °C and (d) 1000 °C.

The power of solid-state annealing is the change in Gibbs free energy (or chemical potential energy) of the collections of ZnWO₄ grains. The minimization of Gibbs free energy creates material transfer between particles through grain boundaries. Therefore, annealing any solid state crystalline material to sufficient temperatures will enable Oswald ripening, i.e., larger grains grow bigger at the expense of smaller grains. The growth of smaller grains to larger ones would reduce the specific surface areas due to the reduction in particle numbers and the elimination in pores, which in turn lead to the deduction in surface defect concentration. Since both the grain-boundary diffusion and the volume diffusion rely heavily upon temperature, the control of temperature is critically important to the particle size and morphology of Eu-doped ZnWO₄. For example, grain growth typically goes exponentially with temperature but only linearly with time at a given temperature. This is the generalized Arrhenius' plot. That is the reason why ZnWO₄ grains grow bigger and bigger when the annealing temperature gets higher and higher.

3.3. Elemental Analysis of Eu-Doped ZnWO₄

Figure 6 illustrates the EDX spectrum of Eu-doped ZnWO₄ precursors subjected to annealing at 800 °C. The X-ray emission peaks at 0.53, 1.02, 1.78, and 2.13 keV can be readily attributed to the characteristic emissions of O (K α_1), Zn (L $\alpha_{1,2}$), W (M α_1), and Au (M α_1), respectively. The two peaks at 5.85 keV and 6.46 keV in Figure 6 are assigned to the characteristic emissions of Eu (L $\alpha_{1,2}$) and Eu (L β_1), respectively. The peak at 8.40 keV is originated from the characteristic emissions of W (L α_1). As a contrast, the peak at 8.64 keV is contributed by the characteristic emissions of Zn(K α_1) at 8.64 keV and Zn (K α_2) at 8.62 keV. Similarly, the characteristic emission of Au (K α_1) at 9.71 keV is merged with that of W (L β_1) at 9.67 keV. As noted previously, the presence of Au element in the specimen was originated from Au sputtering for SEM analysis [29,30]. It can be seen clearly that elements Zn, O, W, and Eu are present in the sample. Thus, it can concluded safely that our sample consists of four kinds of chemical elements Zn, O, W, and Eu. Furthermore, the atomic percentages of the chemical elements can also be quantitatively derived on the basis of the EDX characterizations. After the removal of Au atoms from consideration, the atomic percentages are calculated to be 22.6 at %, 26.5 at %, 49.0 at % and 1.90 at % for elements Zn, W, O and Eu, respectively. The precision of the data is $\pm 0.04\%$. For Eu-doped ZnWO₄ grains with doping level of 5 mol %, the ideal atomic percentages are 16.53 at %, 16.53 at %, 66.11 at % and 0.83 at % for elements Zn, W, O, and Eu, respectively. Obviously, the EDX technique is able to give a rough quantification of dopants in ZnWO₄ phosphors.

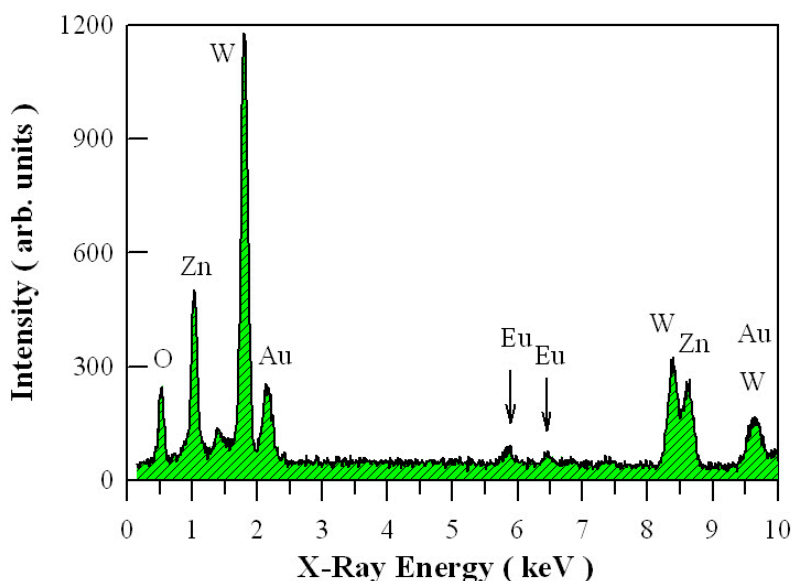


Figure 6. EDX spectrum of Eu-doped ZnWO₄ precursors subjected to annealing at 800 °C for 2 h.

3.4. X-ray Photoelectron Spectroscopic Characterization of Eu-Doped ZnWO₄ Grains

Ionic Eu can exist in the valence state of Eu³⁺ or Eu²⁺ [21,22]. Therefore, we have to explore the chemical states of Eu ions in the phosphors. High-resolution XPS spectra are shown in Figure 7 for Zn 2p, O 1s, W 4f, and Eu 3d in Eu-doped ZnWO₄ nanoparticles derived by annealing the precursor at 400 °C. As can be seen clearly in Figure 7a, the XPS peaks of Zn 2p_{3/2} at 1021.88 eV and Zn 2p_{1/2} at 1044.98 eV correspond to the typical Zn²⁺ oxidation states in ZnWO₄ nanoparticles. As shown in Figure 7b, the peak of the XPS spectrum of O 1s is located at 530.88 eV. Detailed analysis shows that this spectrum has two components. The first component is peaked at 530.80 eV and the second component is peaked at 531.52 eV. The second component, which is centered at 531.52 eV, can be attributed to the oxygen vacancies in ZnWO₄. Figure 7c indicates that the XPS peaks of W 4f_{7/2} at 35.38 eV and W 4f_{5/2} at 37.48 eV can be assigned to W 4f_{7/2} and W 4f_{5/2}, respectively. In particular, Figure 7d reveals that Eu ions exist in ZnWO₄ grains in the form of mixed valence states. As shown in Figure 7d, four peaks can be identified at 1124.78, 1134.58, 1155.18, and 1163.88 eV. According to previous reports, the first two peaks in Figure 7d can be assigned to Eu²⁺ (3d_{5/2}) and Eu³⁺ (3d_{5/2}) core-levels whilst the last two peaks in Figure 7d can be assigned to Eu²⁺ (3d_{3/2}) and Eu³⁺ (3d_{3/2}) core-levels, respectively [31,32]. The binding energy of Eu²⁺(3d_{5/2}) is 30.4 eV lower than that of Eu²⁺ (3d_{3/2}), and the binding energy of Eu³⁺(3d_{5/2}) is 29.3 eV lower than that of Eu³⁺(3d_{3/2}). The area ratios of the XPS signals are approximately 1.48:5.15:1.00:3.37 for Eu²⁺(3d_{5/2}): Eu³⁺(3d_{5/2}): Eu²⁺(3d_{3/2}): Eu³⁺ (3d_{3/2}). With a standard of Eu²⁺ doped ZnWO₄ (doping level 1 mol %), we measured its high-resolution XPS spectrum of Eu 3d_{3/2} and Eu 3d_{5/2}. The peak areas of Eu²⁺ (3d_{5/2}) and Eu²⁺ (3d_{3/2}) are obtained by area integration of the spectrum. The comparison of the peak areas of Eu²⁺ (3d_{3/2}) and Eu²⁺ (3d_{5/2}) in Figure 7d with those of the reference sample, the concentration of Eu²⁺ in the Eu-doped ZnWO₄ nanoparticles can be determined. In this way, the concentration of Eu²⁺ in Eu-doped ZnWO₄ nanoparticles is derived to be 0.9 mol %, leaving the concentration of Eu³⁺ in Eu-doped ZnWO₄ to be 4.1 mol %. Consequently, the data in Figure 7d point out the presence of Eu²⁺ and Eu³⁺ in ZnWO₄ nanoparticles, although Eu³⁺ ions are the only doping source in the starting materials. Consequently, a fraction of Eu³⁺ ions must be self-reduced to Eu²⁺ ions [22].

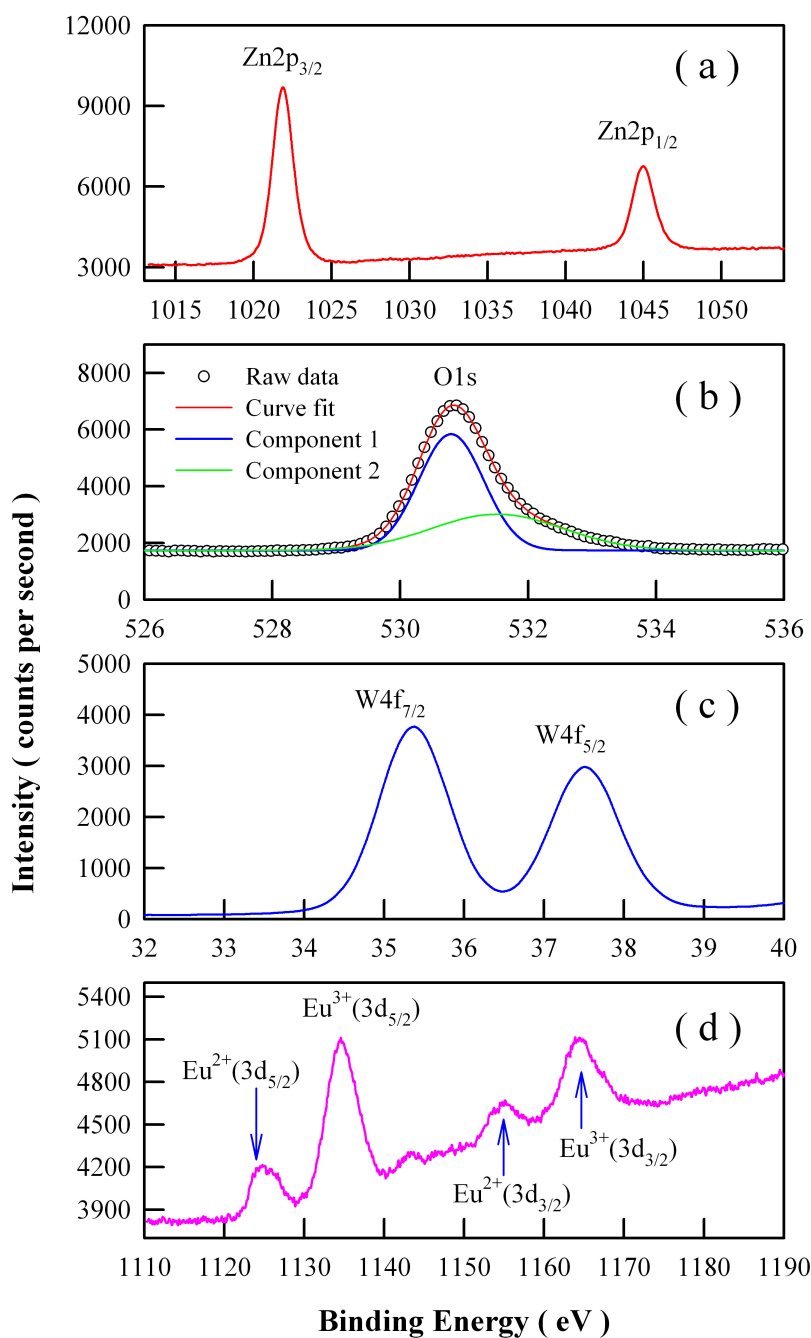


Figure 7. High-resolution XPS spectra of Eu-doped ZnWO₄ precursors subjected to annealing at 400 °C: (a) Zn2p_{3/2} and Zn2p_{1/2}; (b) O1s; (c) W4f_{7/2} and W4f_{5/2}; (d) Eu3d_{3/2} and Eu3d_{5/2}.

It is known that oxygen vacancy (V_O) can be easily produced in the lattice of ZnWO₄ in the crystal growth phase. As one V_O is formed in ZnWO₄, one positively charged V_O is left in the lattice. In the meanwhile, one negatively charged oxygen species is released into the lattice in order to keep the lattice neutral. When the negatively charged oxygen species diffuses randomly in the lattice, it donates its electrons with the liberation of oxygen out of the lattice. This process can be described by Equation (1)



In this way, the vacancy V_O would act as a donor of electrons. Eu^{3+} ion can be reduced to Eu^{2+} by capturing the released electron. A detailed discussion on the self-reduction of Eu^{3+} to Eu^{2+} can be found elsewhere [22], and this process can be described by Equation (2)



3.5. Photoluminescence Spectra of Eu-Doped ZnWO_4 Phosphors

Figure 8 depicts the PL spectra of Eu-doped ZnWO_4 precursors subjected to annealing at 400, 600, 800, and 1000 °C. The open circles in Figure 8 represent the raw PL data. The general feature in Figure 8 is that each PL spectrum is composed of a broad PL band centered at about 480 nm and the three sharp emissions peaking at 590, 612, and 625 nm, respectively. It is known that trivalent rare-earth ions are characterized by an electronic structure consisting of an unfilled inner 4f shell and outer filled 5s and 5p shells. When these trivalent rare-earths are present in a solid, the effects of the crystalline field are a small perturbation on the 4f states because of the shielding of the outer electron shells. Since the interaction with host is weak, their emission spectrum is nearly independent of host lattice. Such kind of host independence was evidenced by the characteristic emissions of Eu^{3+} , Tb^{3+} , and Dy^{3+} in a variety of hosts [21,22,24,28–30,33]. The other feature of trivalent rare-earth ions is that their 4f–4f transitions are parity forbidden. In the case of Eu^{3+} , the electric-dipole transitions between the 5D_0 and 7F_2 states of Eu^{3+} ion are parity-forbidden although the much weaker magnetic dipole transition between 5D_0 and 7F_1 is allowed. In practice, however, it turns out that intra-configurational electric-dipole transitions are often dominant since even a small admixture with odd symmetry components to the electronic wave-function of 4f configuration causes significant changes in the transition probabilities and allows the electric-dipole transitions. Therefore, the dominant peak centered at about 612 nm in Figure 8 can be attributed to the hypersensitive $^5D_0 \rightarrow ^7F_2$ transition of Eu^{3+} ions in ZnWO_4 lattice whereas the peak with low intensity at about 590 nm is assigned to the $^5D_0 \rightarrow ^7F_1$ transition. It can be clearly seen that the peak intensity of the dominant electric-dipole transition is much larger than that of the magnetic dipole transition, demonstrating that Eu^{3+} ion occupies non-centrosymmetric sites in the host lattice.

Each of the broad PL band in Figure 8 can be decomposed into two Gaussian components according to Equation (3)

$$I(\lambda) = I_1 \exp \left[-\frac{(\lambda - \lambda_1)^2}{2\sigma_1^2} \right] + I_2 \exp \left[-\frac{(\lambda - \lambda_2)^2}{2\sigma_2^2} \right] \quad (3)$$

where $I(\lambda)$ is the PL intensity recorded at wavelength λ ; I_1 , λ_1 and σ_1 are the pre-exponential factor, mean value and standard derivation of the first Gaussian component, respectively. Meanwhile, I_2 , λ_2 , and σ_2 are the pre-exponential factor, mean value, and standard derivation of the second Gaussian component, respectively [34]. For brevity, the first Gaussian component is denoted as the blue PL component whilst the second Gaussian component is denoted as the green PL component, which are represented by the solid blue curve and the solid green curve for each PL spectrum in Figure 8, respectively. The red curve in each panel is the sum of the two components. The fitting parameters of the two-component Gaussian decomposition of the PL spectra are listed in Table 2. The most striking feature in Figure 8 is the coexistence of the blue PL component and green PL component, which suggests the presence of two kinds of distinctly different luminescence centers in ZnWO_4 . The second most striking feature in Figure 8 is that both the peak positions and the PL intensities of the two PL components are annealing temperature dependent. For example, the peak position of the blue PL component varies in the range of 448.12 to 470.69 nm in the meanwhile the peak position of the green PL component varies in the range of 504.19 to 538.08 nm. Moreover, with respect to red emissions of Eu^{3+} at 612 nm, the PL intensity of ZnWO_4 host increases gradually to its maximum as the annealing temperature increases from 400 through 600 to 800 °C, and then it turns its head down as the annealing

temperature is increased further from 800 to 1000 °C. The annealing temperature dependent PL bears significance in defect engineering of the emissions from ZnWO₄ host. For instance, it can be employed to realize color tunable emissions if the blue emissions from ZnWO₄ host are combined to the red emissions from Eu³⁺ ions.

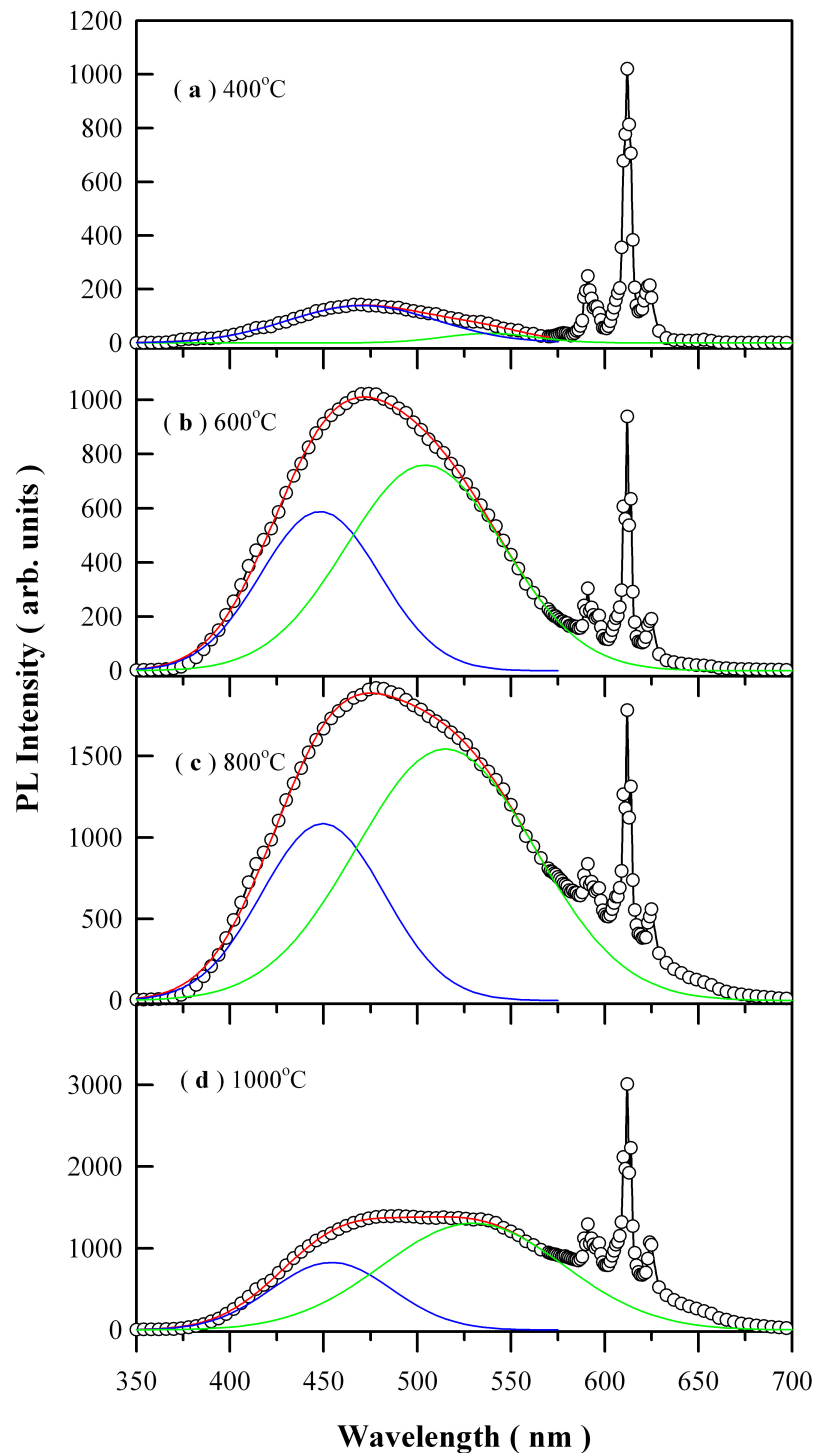


Figure 8. PL spectra of Eu-doped ZnWO₄ precursors subjected to annealing at different temperatures: (a) 400 °C; (b) 600 °C; (c) 800 °C; and (d) 1000 °C. The blue curve and the green curve stand for the blue and green components of Gaussian decomposition, respectively. The red curve is the sum of the two components. The excitation wavelength was 325 nm.

Table 2. Parameters of two-component Gaussian decomposition of the PL spectra of Eu-doped ZnWO₄ precursors subjected to annealing at different temperatures.

<i>T</i> (°C)	Blue Component			Green Component		
	<i>I</i> ₁	λ_1 (nm)	σ_1 (nm)	<i>I</i> ₂	λ_2 (nm)	σ_2 (nm)
400	13,945.13	470.69	39.58	3521.63	538.08	24.63
600	58,868.43	448.12	31.74	75,969.80	504.19	42.04
800	108,589.98	449.59	32.65	154,290.49	515.02	47.58
1000	82,666.25	454.16	32.06	130,656.84	529.70	48.36

The broad PL band from ZnWO₄ host is often attributed to the charge transfer between oxygen and tungsten ions in [WO₆]⁶⁻ molecular complex [1]. However, such assignment is quite elusive for physicists. In the view of solid-state physics, the origins of PL can be classified into band edge emission and defect emission. Due to the large difference between the bandgap of ZnWO₄ (about 4 eV) and its emission energy (around 2.6 eV), we can exclude the possibility of band edge recombination as the candidate of the broadband emissions of ZnWO₄ grains. In actual cases, defect emissions often dominate the PL properties in diverse metal oxides such as HfO₂ [35], Zn₅Mo₂O₁₁ [28], SrAl₂O₄ [36,37], BaAl₂O₄ [33], and ZnMO₄ [38]. This also holds true for ZnWO₄ grains, where coordinatively unsaturated vacancies are active sites for luminescence. This feature allows us to assign the broad PL band peaking at about 480 nm to certain kinds of defects in ZnWO₄. The most common defects in ZnWO₄ include O, W, and Zn vacancies, which are likely candidates of the luminescence centers. Although the relation between the intrinsic defects and the luminescence centers in ZnWO₄ are not clearly identified yet, the PL spectra in Figure 8 demonstrate that the PL properties of ZnWO₄ host are highly governed by the number and the kind of defects in ZnWO₄ lattice. The role of Eu³⁺ doping is to provide the red emission so that tunable PL from blue to red can be realized by combining the blue-green emission from ZnWO₄ host with the red emission from Eu³⁺ dopant. Without the red emission from Eu³⁺ dopant, the emission color of ZnWO₄ host can be tuned only in the blue-green spectral regime. Instead of varying the concentration of Eu³⁺ ions in ZnWO₄, this work shows how to harness the defect engineering in ZnWO₄ to achieve color tunable emissions even when the doping concentration is fixed.

3.6. Color Coordinates of Eu-Doped ZnWO₄

Once the PL spectrum of Eu-doped ZnWO₄ phosphors is modified by the control of annealing temperature, the perception color will be changed correspondingly. On the basis of the PL spectral data, the chromaticity coordinates can be calculated in the Commission Internationale de L'Eclairage (CIE) 1931 XYZ color space [28]. Figure 9 depicts the evolution of the luminescence color of Eu-doped ZnWO₄ precursors with annealing temperature. The solid line in Figure 9 is for eye guidance only. After annealing at 400 °C for 2 h, the luminescence color of the phosphor is purplish pink with its color coordinates of (0.333, 267). After annealing at 600 °C for 2 h, the luminescence color of the phosphor is changed to greenish blue with its color coordinates of (0.193, 0.242). After annealing at 800 °C for 2 h, the luminescence color of the phosphor is also greenish blue with its color coordinates of (0.223, 0.284). After annealing at 1000 °C for 2 h, the luminescence color of the phosphor is white with its color coordinates of (0.280, 0.331). Among the four phosphors, the chromaticity coordinates (0.280, 0.331) are very close to the achromatic point whose coordinates are (0.333, 0.333). It is known that white light-emitting phosphors are critically important in solid state lighting industry. There is reason to believe that white light emissions can be achieved in Eu-doped ZnWO₄ phosphors by fine adjustment of the annealing temperature. Our work demonstrates that color tunable emissions can be achieved by thermal annealing the phosphors at different temperatures. Rather than controlling the doping concentration of Eu³⁺ ion [5,8,13–15], the color tunable PL from Eu-doped ZnWO₄ is realized by engineering the intrinsic defect emissions from ZnWO₄ lattice through variations of annealing temperature. Therefore, the strategy of tuning the emission color of Eu-doped ZnWO₄ turns out to be a

strategy on how to control the intrinsic defects in ZnWO_4 in an environmentally friendly, cost-effective, scalable, and controllable manner.

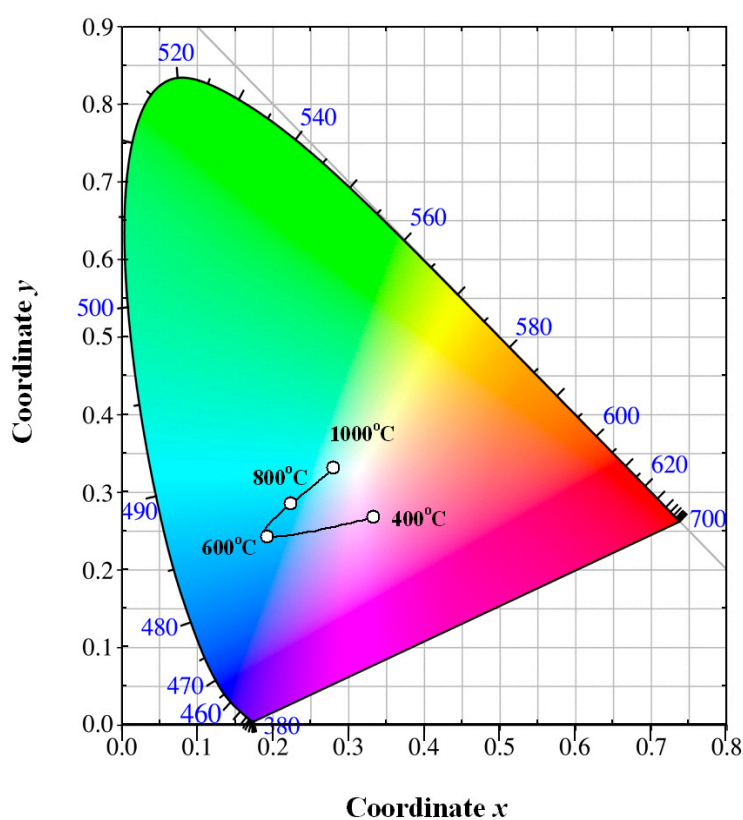


Figure 9. Commission Internationale de L'Eclairage chromaticity diagram of Eu-doped ZnWO_4 precursors subjected to annealing at different temperatures.

The annealing temperature dependent PL suggests the feasibility to tune the PL color of Eu-doped ZnWO_4 . Figure 10 shows the luminescence photos of Eu-doped ZnWO_4 precursors subjected to annealing at 400, 600, 800, and 1000 °C. The calculated color coordinates are displayed in each photo. It is obvious in Figure 10 that the luminescence color of Eu-doped ZnWO_4 depends on the annealing temperature. In our case, tunable color is realized by mixing the blue emissions from ZnWO_4 lattice with the red emissions from Eu^{3+} ions. Such a change in the luminescence color can be understood when we refer to the dramatic changes in the broadband PL intensity as the annealing temperature increases from 400 to 1000 °C. In a similar way, Zhai et al. reported that white light-emitting can be obtained by combining the bluish emission of tungstate group with the characteristic emission of Eu^{3+} and Dy^{3+} [15]. With the method described earlier [21], the correlated color temperatures are calculated to be 5437, 50,758, 18,053, and 8437 K for the four Eu-doped ZnWO_4 phosphors which were annealed at 400, 600, 800, and 1000 °C, respectively. Our work demonstrates that the emission color of Eu-doped ZnWO_4 can be manipulated over a significant range through variations of the annealing temperature.

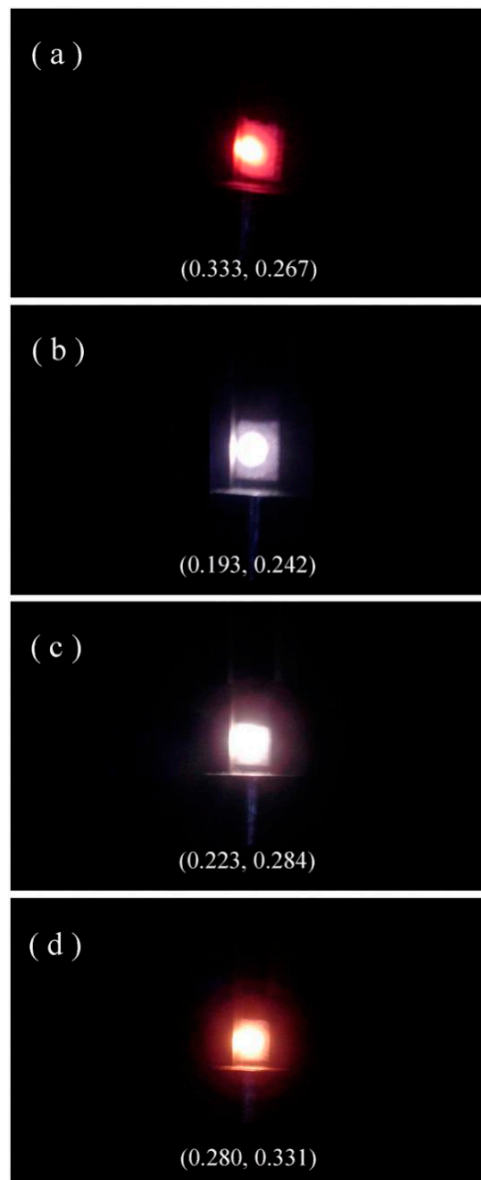


Figure 10. Luminescence photos of Eu-doped ZnWO₄ precursors subjected to annealing at different temperatures: (a) 400 °C; (b) 600 °C; (c) 800 °C; and (d) 1000 °C.

3.7. Electronic Structures of Perfect ZnWO₄ and Defect-Containing ZnWO₄

Many kinds of defects are present in practical solids. Examples of the intrinsic defects in ZnWO₄ include vacancies (O vacancy, Zn vacancy, W vacancy), interstitials (O interstitial, Zn interstitial, W interstitial) and antisites (O antisite, Zn antisite, W antisite), etc. After having considered the high formation energies of antisites, the three kinds of vacancies are the most probable intrinsic defects in ZnWO₄ with sufficiently high population. Even in the absence of doping agent Eu³⁺ ions, O, W, and Zn vacancies occur naturally in the lattice of ZnWO₄ at any given temperature up to the melting point of the material. A Kröger–Vink representation of Schottky defect formation in ZnWO₄ can be described by Equation (4)



It can be seen in Equation (4) that V_O can act as electron trap since it is positively charged. Similarly, both Zn vacancy and W vacancy can act as hole trap since they are negatively charged. As discussed above, intrinsic defects in ZnWO₄ have played important roles in the broadband

emissions. Therefore, the electronic structures of intrinsic defects in ZnWO_4 are critically important to understand the absorption and luminescent properties of ZnWO_4 . Density functional calculations can be reliably applicable to the electronic structure calculations for a variety of materials [21,23,24,30]. In the framework of GGA+U, we performed electronic structure calculations for perfect ZnWO_4 and defect-containing ZnWO_4 by defining $U^{5d} = 10$ eV for W.

Figure 11 presents the calculated band structures and density of states of perfect ZnWO_4 . As shown in Figure 11a, both the maximum of valence band (VB) and the minimum of conduction band (CB) are located at Z point, confirming that ZnWO_4 is a semiconductor with direct bandgap. The bandgap value is derived to be 4.04 eV. Moreover, it can be seen that some bands at the bottom of CB are not flat, which is the typical character of a semiconductor. In principle, the bandgap value can also be calculated from the density of states of defect-free ZnWO_4 . On the basis of the density of states shown in Figure 11b, the calculated bandgap is 4.04 eV, too, for defect-free ZnWO_4 . The most prominent feature in Figure 11b is that the bandgap of ZnWO_4 is free of any impurity energy levels. The second most prominent feature in Figure 11b is that perfect ZnWO_4 possesses remarkably sharp band edges. On the basis of ab initio study, Kalinko et al. reported that ZnWO_4 is a direct semiconductor with its bandgap value of around 2.31 eV [39]. In our GGA+U calculations, the bandgap values are 2.64, 2.87, 3.12, 3.41, 3.72, and 4.04 eV when $U^{5d} = 0, 2, 4, 6, 8, 10$ eV for W, respectively. So $U^{5d} = 10$ eV is the best value to fit the experimental bandgap data. By measuring the diffuse reflectance spectrum of ZnWO_4 film coated on quartz substrate, Zhao et al. reported that the experimental bandgap of the ZnWO_4 film was about 4.01 eV [40]. It can be seen that our derived bandgap value is in reasonable agreement with the experimental bandgap value reported by Zhao et al.

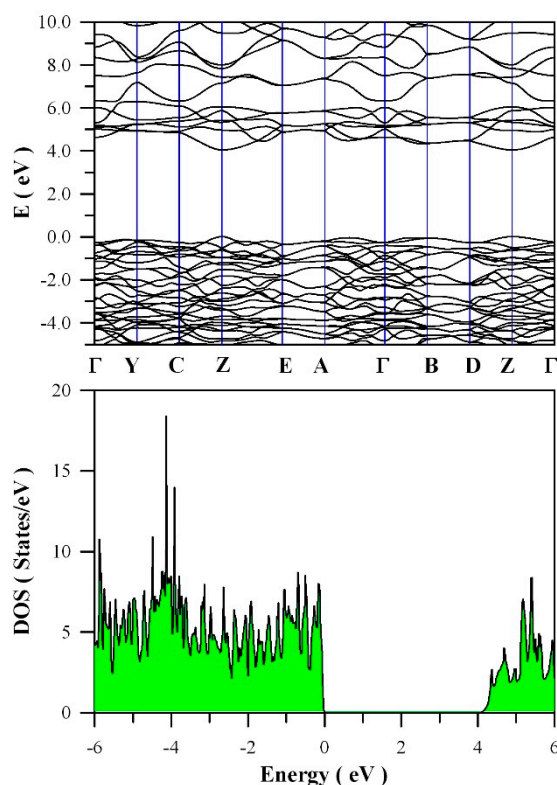


Figure 11. DFT calculated electronic structures for defect-free ZnWO_4 : (a) band structures; (b) density of states.

V_O is one of the most fundamental defects in ZnWO_4 , it influences many physical properties of the material such as charge trapping and recombination. Therefore, detailed knowledge of the electronic structures of V_O is essential in understanding the PL of ZnWO_4 . In order to model V_O in ZnWO_4 , we built a $2 \times 2 \times 2$ super cell which contains 64 O sites, 16 W sites and 16 Zn sites. After one O site

was removed from this super cell, oxygen deficient ZnWO_4 is resulted with the atomic concentration of V_{O} in ZnWO_4 up to 1 at %. For simplicity, this oxygen deficient ZnWO_4 is denoted as $\text{ZnWO}_{4-\delta}$ where $\delta = 0.0625$. Figure 12 represents the calculated band structures and density of states of oxygen deficient ZnWO_4 . As shown in Figure 12a, the calculated bandgap of V_{O} bearing ZnWO_4 is 4.04 eV when $U^{5d} = 10$ eV for W. The most prominent feature in Figure 12 is that V_{O} can introduce two defect energy levels in the bandgap of ZnWO_4 , one of which is located at $E_{\text{V}} + 1.85$ eV whilst the other is located at $E_{\text{V}} + 3.71$ eV. The two defect energy levels are clearly marked in red, as shown Figure 12b. Since it is positively charged, V_{O} can act as electron trap sites as well as luminescence center as they do in HfO_2 [35].

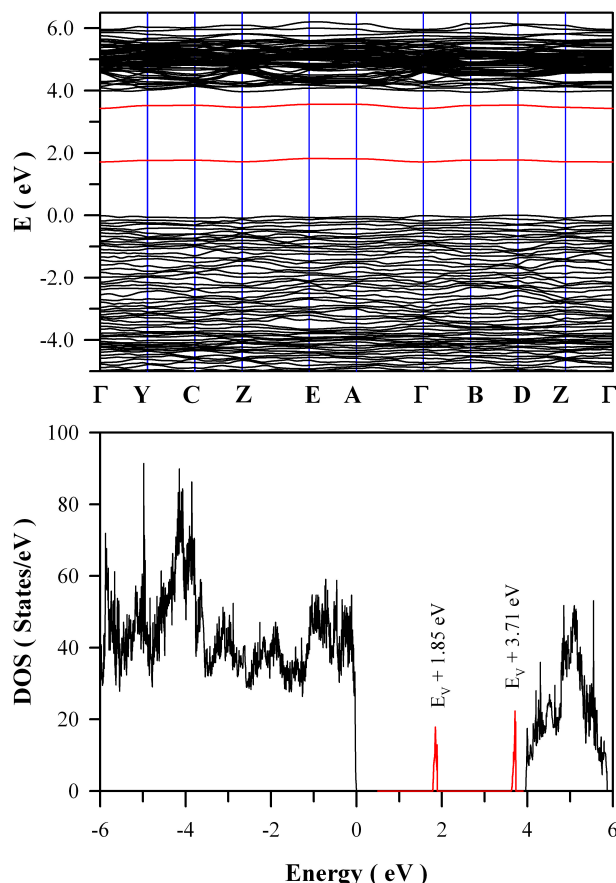


Figure 12. Density functional theory (DFT) calculated electronic structures for oxygen deficient ZnWO_4 ($\text{ZnWO}_{4-\delta}$ where $\delta = 0.0625$): (a) band structure; and (b) density of states.

Besides V_{O} , tungsten vacancy (V_{W}) can be also present in ZnWO_4 . Understanding the electronic structures of V_{W} quantitatively is important for developing this family of materials for potential applications, which include emission color tunable phosphors. In order to model V_{W} in ZnWO_4 , we built a $2 \times 2 \times 2$ super cell which contains 64 O sites, 16 W sites and 16 Zn sites. After one W site was removed from this super cell, tungsten deficient ZnWO_4 is resulted with the atomic concentration of V_{W} in ZnWO_4 up to 1 at %. For simplicity, this tungsten deficient ZnWO_4 is denoted as $\text{ZnW}_{1-\delta}\text{O}_4$ where $\delta = 0.0625$. Figure 13 shows the calculated band structures and density of states of tungsten deficient ZnWO_4 . As can be seen in Figure 13a, the bandgap remains direct with the value of 4.05 eV. In contrast to the clean bandgap of perfect ZnWO_4 , the bandgap of tungsten deficient ZnWO_4 contains a lot of defect energy levels. It can be seen clearly in Figure 13b that the defect energy levels created by V_{W} span from $E_{\text{V}} + 0.1$ eV to $E_{\text{V}} + 0.7$ eV, where the V_{W} introduced defect energy levels are marked in blue. The peak of V_{W} created band is located at $E_{\text{V}} + 0.62$ eV. Since it is negatively charged, V_{W} can act as hole trap sites as well as luminescence center.

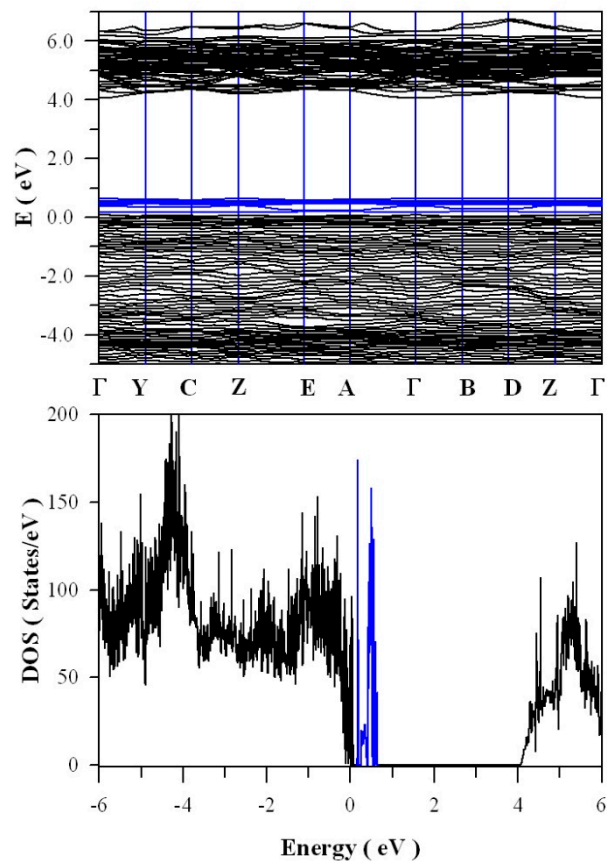


Figure 13. DFT calculated electronic structures for tungsten deficient ZnWO_4 ($\text{ZnW}_{1-\delta}\text{O}_4$ where $\delta = 0.0625$): (a) band structure; and (b) density of states.

As the other typical defect, zinc vacancy (V_{Zn}) can be present in ZnWO_4 . Being negatively charged, V_{Zn} can also act as charge carrier traps and luminescence centers. Therefore, we have to take the Zn defect states into account in order to understand the defect emissions from ZnWO_4 . In order to model V_{Zn} in ZnWO_4 , we built a $2 \times 2 \times 2$ super cell which contains 64 O sites, 16 W sites, and 16 Zn sites. After one zinc site was removed from this super cell, zinc deficient ZnWO_4 is resulted with the atomic concentration of V_{Zn} in ZnWO_4 lattice up to 1 at %. For simplicity, this tungsten deficient ZnWO_4 is denoted as $\text{Zn}_{1-\delta}\text{WO}_4$ where $\delta = 0.0625$. Figure 14 shows the calculated band structures and density of states of zinc deficient ZnWO_4 . As marked in pink in Figure 14a, there are some zinc defect energy levels in the bandgap of ZnWO_4 , but they are very close to the top of VB (<0.1 eV). From a perfect Zn site, the Kröger–Vink notation for the defect reactions of V_{Zn} in ZnWO_4 can be described by Equation (5)



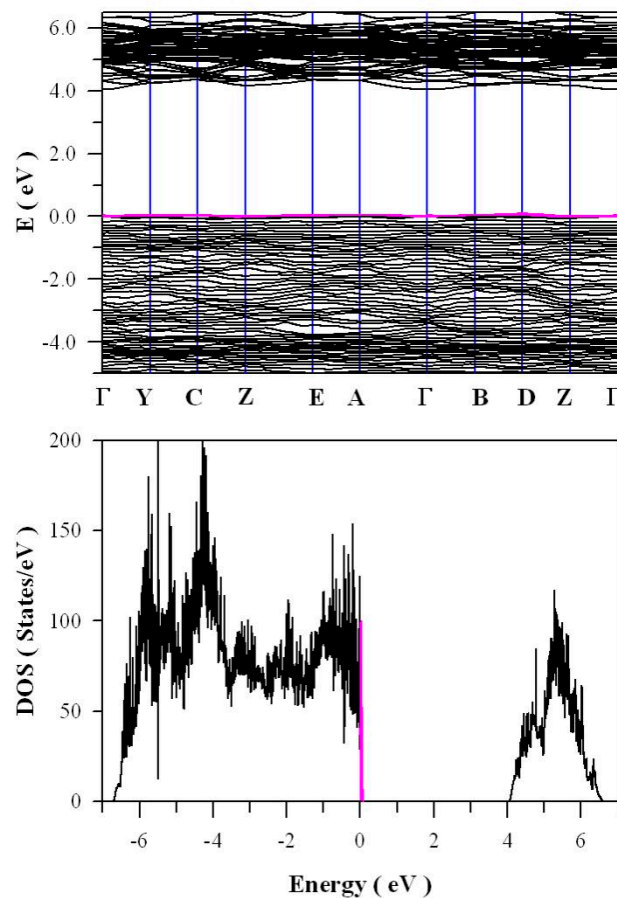


Figure 14. DFT calculated electronic structures for zinc deficient ZnWO_4 ($\text{Zn}_{1-\delta}\text{WO}_4$ where $\delta = 0.0625$): (a) band structure; and (b) density of states.

In Equation (5), the masses, sites and charges are balanced for the intrinsic defects. Equation (5) indicates that the creation of a V_{Zn} from a zinc site in ZnWO_4 yields one negatively charged defect V_{Zn} and one positively charged zinc interstitial defect. The creation of a V_{Zn} is quite similar to the p-type doping silicon with phosphorus since positive charges are released into the host lattice. Obviously, the negatively charged V_{Zn} can work as an acceptor with the capability of trapping holes in ZnWO_4 . It is interesting to note that the acceptor levels in the forbidden band are closely packed above the VB of ZnWO_4 . This phenomenon can be understood in the light of weak interaction between the zinc interstitial defect and the negatively charged V_{Zn} . The low ionization energy for the release a zinc interstitial defect is responsible for are closed packed zinc defect energy levels just above the VB of ZnWO_4 .

Belong to 4f–5d transition, Eu^{2+} doped nanomaterials generally show a broad PL band ranging from ultraviolet through visible to infrared regime. However, Eu^{2+} doped ZnWO_4 grains exhibit no extra PL band in the visible range when compared to undoped ZnWO_4 grains. We recorded the PL spectrum of Eu^{2+} doped ZnWO_4 with the 325 nm excitation wavelength. Figure 15a shows the PL spectrum of Eu^{2+} doped ZnWO_4 with the doping concentration of 1 mol %. When compared to the PL spectrum of Eu^{3+} doped ZnWO_4 as shown in Figure 15b, we can see that the presence of Eu^{2+} does not introduce an extra PL band in the visible spectral regime. It is possibly due to the low amount of Eu^{2+} ions in ZnWO_4 . Further exploration is required to study the Eu^{2+} emission in ZnWO_4 host. As for Eu^{3+} doped ZnWO_4 , the 4f electrons of the dopant are sufficiently localized to form multiple atomic-like states in the bandgap of ZnWO_4 due to the shielded 4f-shell. Since the DFT calculations are one-electron theory, the DFT with GGA scheme fails to accurately predict the multi-electron properties of Eu^{3+} ions in ZnWO_4 . Consequently, neither the energies of J multiplets of Eu^{3+} ions (7F_J , where

$J = 0-6$) in the ground state nor the energy levels in the excited state (5D_0) of Eu^{3+} ions can be deduced correctly from the DFT calculations. That is why we did not model the defect energy levels of Eu^{3+} in ZnWO_4 . Fortunately, both the energy levels of Eu^{3+} in ground state and in excited state vary by only a small amount in different hosts. Thus, the energy levels of 7F_J and 5D_0 of Eu^{3+} in ZnWO_4 can be determined by making use of the experimentally obtained energies for Eu^{3+} . The only exception is that the exact location of the lowest energy level of Eu^{3+} (7F_0) is unknown for the case of ZnWO_4 . Additionally, the PL spectrum of Eu^{3+} doped ZnWO_4 with a better resolution is shown in Figure 15b. The excitation wavelength is 325 nm. It can be seen that the $^5D_0 \rightarrow ^7F_0$ emission peak is located at about 582 nm although it is very low in intensity.

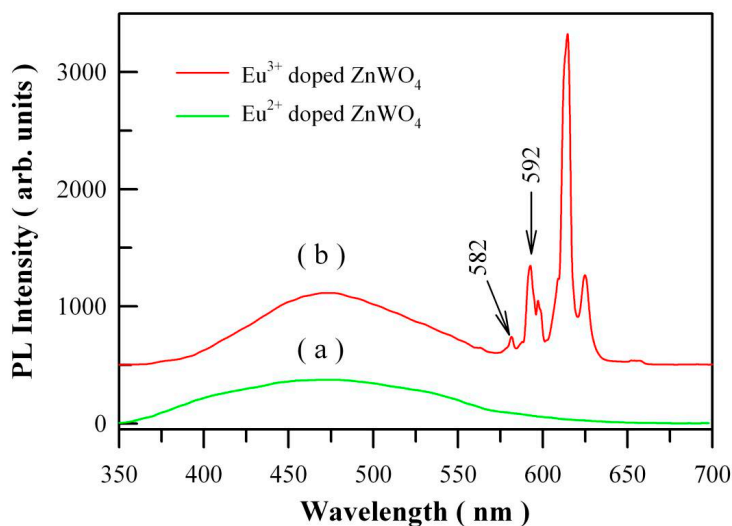


Figure 15. (a) PL spectrum of Eu^{2+} doped ZnWO_4 with the doping concentration of 1 mol %; (b) PL spectrum of Eu^{3+} doped ZnWO_4 with high resolution to show the $^5D_0 \rightarrow ^7F_0$ emission. The excitation wavelength was 325 nm.

3.8. Defect Absorption of Eu-Doped ZnWO_4

Optical absorption spectroscopy is one of the most significant experimental techniques to investigate the optical absorption of defects in semiconducting crystals. In semiconductors, photoexcitation often results in strong band-edge absorption, and optical absorption of defects in semiconducting crystals is often observed in the ultraviolet and visible spectral regime. Figure 16 represents the absorption spectra of Eu-doped ZnWO_4 precursors subjected to annealing at 400, 600, 800, and 1000 °C. As shown Figure 16, an extra absorption band appears in the range of 300–400 nm with its center at around 350 nm. Being superposed the strong absorption of ZnWO_4 host, this absorption band is relatively weak in intensity as the annealing temperature is 400 °C, but it becomes stronger in intensity as the annealing temperature gets higher to 600 °C. When the annealing temperature is raised to 800 °C, the extra absorption band reaches its maximum, as shown in Figure 16c. After that, this extra absorption band starts to lose its intensity when the annealing temperature is elevated further to 1000 °C. It is noted that the peak position of this absorption band does not shift with the annealing temperature although dramatic changes in the absorption intensity are recorded. Alongside with the absorption spectra, the insets in Figure 16 illustrate the Tauc plots of the Eu-doped ZnWO_4 phosphors. The optical bandgaps of the Eu-doped ZnWO_4 phosphors, as indicated by the solid pink lines in the Tauc plots, are very close to 4.0 eV. Additionally, the defect absorptions can be seen clearly in the Tauc plots, too. As compared to others, the absorbance behavior of the curve at 800 °C is particular because the defect absorption band is so strong that the band-edge absorption is severely depressed. This case suggests that the defect concentration in ZnWO_4 reaches the maximum. Therefore, the data in Figure 16 indicate that the defect concentration in ZnWO_4 phosphors increases

with the annealing temperature until it reaches to maximum at 800 °C. Then the defect concentration in ZnWO₄ phosphors decreases as the annealing temperature increases further to 1000 °C.

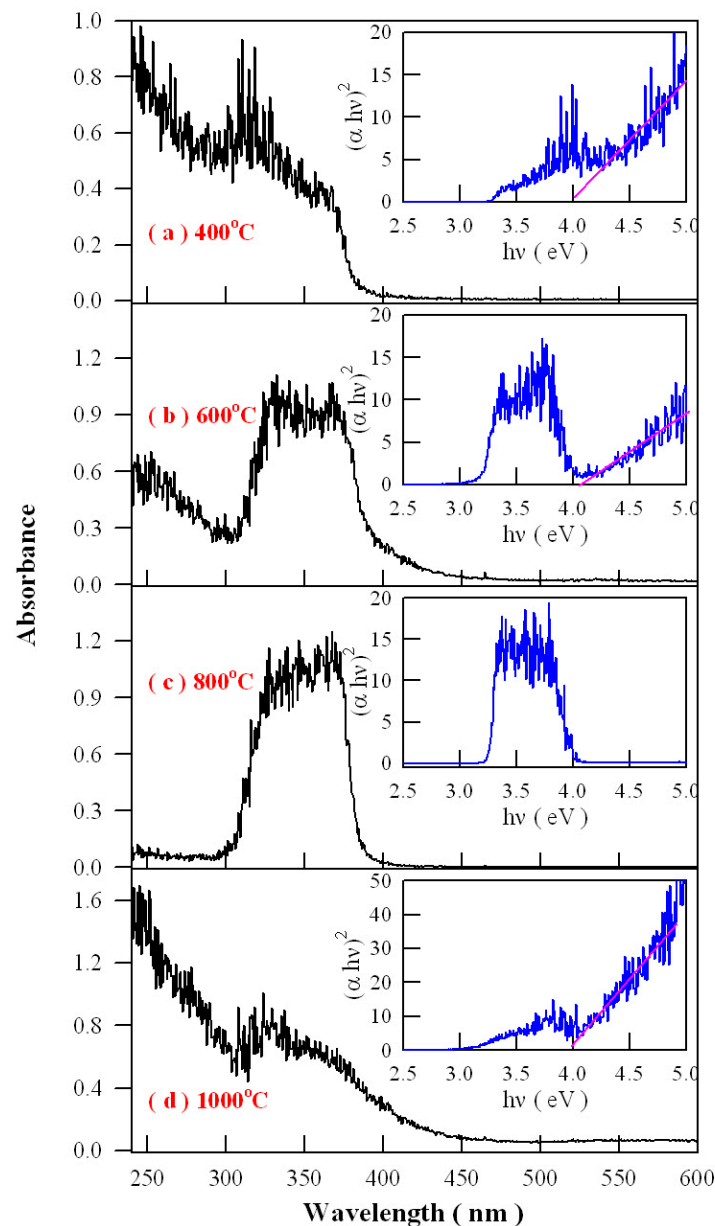


Figure 16. Absorption spectra of Eu-doped ZnWO₄ precursors subjected to annealing at different temperatures: (a) 400 °C; (b) 600 °C; (c) 800 °C; and (d) 1000 °C. Inset: Tauc plots to derive bandgap values.

Analysis of the intensity, width, and shape of the extra absorption band sometimes can yield a lot of information about the defect absorption in ZnWO₄. The defect absorption band is centered at about 350 nm (3.54 eV). It is clear that the intensity of the extra absorption band heavily depends on the annealing temperature. When referred to defect energy levels of V_O shown in Figure 12, it is found that this absorption band coincides in energy with the transition from VB to the defect level of V_O at E_V + 3.71 eV. Moreover, for condensed matter and solids, the shape of absorption bands are determined by the density of states of the initial state and the density of states of the final states that are involved into electronic transitions. The comparison of the extra absorption band in Figure 16 with the calculated DOS in Figure 11 clearly discloses that this absorption band is due to electronic transition from VB to

the deep donor level of V_O at $E_V + 3.71$ eV. Consequently, the data in Figure 16 give evidence of V_O related defect absorption at about 350 nm.

Thermal annealing is the process of subjecting a substance to the action of heat, but without melting or fusion, for the purpose of causing some change in its physical or chemical constitution. In our case, thermal annealing generates numerous defects in $ZnWO_4$. It is well established that the population density of V_O in a solid increases quickly with the increase in annealing temperature according to Equation (6)

$$n = A \exp(-Q_V/kT) \quad (6)$$

where n is the population density of V_O in the solid, A is the proportionality constant, Q_V is activation energy for vacancy formation of V_O in the host, T is the absolute temperature in Kelvin, and k is the Boltzmann constant [22]. It can be seen from Equation (6) that high population density of V_O can be easily created in $ZnWO_4$ when the annealing temperature is elevated. For this reason, the V_O related absorption band gets stronger in intensity after having been annealed at a higher temperature. The higher the annealing temperature is, the more V_O is produced in $ZnWO_4$, which result in stronger defect absorption. It is worthwhile to note that the population density in Equation (6) stands for the population density of volume defects in $ZnWO_4$ but not the population density of surface defects on $ZnWO_4$ grains. Actually, the surface defects cannot be neglected in our case. As shown in Figure 5, the mean particle size of $ZnWO_4$ grains increases from 80 nm to 20 μ m as the annealing temperature increase from 400 to 1000 $^{\circ}$ C. At a given volume, the surface area of $ZnWO_4$ grains derived at 1000 $^{\circ}$ C is about 1/4000 of the surface area of $ZnWO_4$ grains derived at 400 $^{\circ}$ C. It is well known that the growth of larger grains would reduce the surface areas by particle number reduction and pore elimination, which inevitably leads to the decrease in the surface defect concentration. Obviously, the increase in the volume defect concentration will be mediated by the rapid decrease in the surface defect concentration as $ZnWO_4$ grains grow bigger and bigger. It is anticipated that the increase in the volume defect is outnumbered by the decrease in surface defects at specific temperature, beyond which the total number of defects in $ZnWO_4$ starts to decline. This is the reason why the defect absorption in Figure 16d is decreased significantly with respect to that in Figure 16c. The annealing temperature dependent defect absorption provides a novel avenue to the control of defect emissions in $ZnWO_4$.

3.9. Possible Mechanism of Tunable PL from Eu-Doped $ZnWO_4$

Figure 17 illustrates the possible mechanism of tunable PL from Eu-doped $ZnWO_4$. As displayed in Figure 17, the bandgap value of $ZnWO_4$ is assumed to be 4.0 eV, the V_O introduced defect energy levels are located at $E_V + 1.85$ eV and $E_V + 3.71$ eV. V_O is positively charged thus it can capture electrons. Meanwhile, V_W introduced defect energy level is located at $E_V + 0.62$ eV. V_W is negatively charged thus it can capture holes. Under the UV excitation, electrons are pumped into the conduction band (CB) of $ZnWO_4$, leaving holes in the VB of $ZnWO_4$. This process is accompanied with strong band-edge absorption, which is shown by the Tauc plots in Figure 16. In addition to the band-edge absorption, defect absorption can sometimes be recorded, too. According to Figure 17, the transition from VB to the defect energy level of V_O at $E_V + 3.71$ eV should yield a defect absorption band peaking at 335 nm. Indeed, this extra absorption band is evidenced by the extra absorption spectra in Figure 16. After photoexcitation, the photo-generated electrons and holes will be relaxed via diverse paths. The first kind of radiative recombination is the electrons trapped by V_O at $E_V + 3.71$ eV to recombine with the holes trapped by V_W at $E_V + 0.62$ eV, resulting in the blue PL band peaking at around 428 nm (2.90 eV). The second kind of radiative recombination is the electrons in CB to recombine with the positively charged V_O at $E_V + 1.85$ eV, yielding the green PL band peaking at around 576 nm (2.15 eV). From this point of view, both the blue component and the green component of the broadband PL spectrum are readily explained. Obviously both the intrinsic defects V_O and V_W are involved into the radiative recombinations. When compared to the energies of the blue and the green PL bands in Figure 8, our predicted emission energies of the defect emissions roughly agree to the experimental values. The differences between the predicted emission energies in Figure 17 and the actual emission

energies in Figure 8 rest on the fact that it is hard to exactly and reliably determine the defect energy levels with DFT calculation due to the limitations in semilocal approximations to DFT. The third kind of radiative recombination is the electrons in the excited state 5D_0 of Eu^{3+} to recombine radiatively with the holes in its ground states $^7F_{1,2}$, leading to the characteristic emissions peaking at 591 and 612 nm.

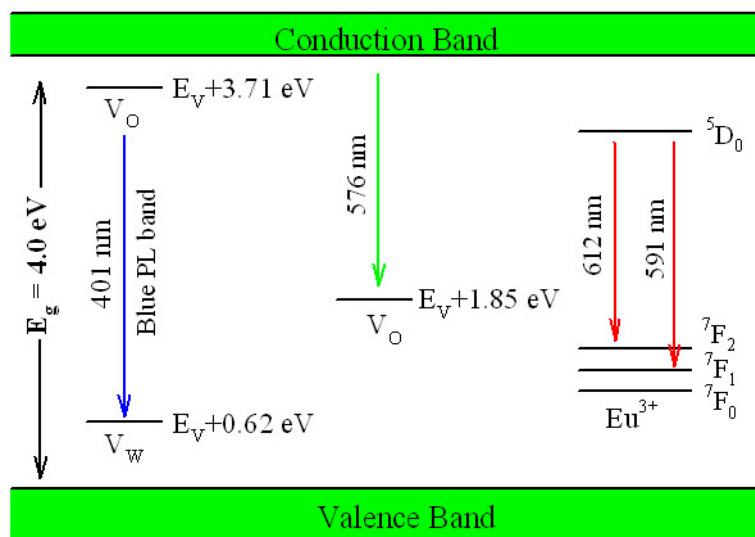


Figure 17. Possible mechanisms of tunable PL from in Eu-doped ZnWO_4 .

In the light of the mechanism proposed in Figure 17, we can understand the color tunable PL from Eu-doped ZnWO_4 . Standard color-mixing uses red, green and blue emissions that are adjusted to deliver the entire range of the color spectrum. In our case, tunable PL from Eu-doped ZnWO_4 uses color mixing of the red emissions from extrinsic defects Eu^{3+} ions with the bluish emissions from intrinsic defects in ZnWO_4 lattice. Since the interaction of rare earth dopants with host is weak, their emission spectra of trivalent rare earth dopants are nearly independent of host lattice. Consequently, how to adjust the output of the bluish emissions from ZnWO_4 lattice has become the task of controlling the intrinsic defect emissions in ZnWO_4 . As disclosed by our DFT calculation and optical absorption, the bluish emissions from ZnWO_4 lattice are originated from intrinsic defects V_O and V_W , whose population densities can be tuned by carefully controlling the annealing temperature. This is the reason why the output of the bluish emissions from ZnWO_4 host can be tuned through the control of annealing temperature. When compared to the strategy of dopant concentration control, our approach is uniquely positioned to adjust the intrinsic defects in ZnWO_4 lattice by the fine control of annealing temperature. This strategy provides new capability of tuning the emissions from rare earth doped ZnWO_4 even when the rare earth doping concentration is fixed.

3.10. Time-Resolved PL Spectra of Eu-Doped ZnWO_4

In order to gain more physical insight on the defect emissions in ZnWO_4 , we studied the time-resolved PL behaviors of Eu-doped ZnWO_4 . Figure 18 depicts the time-resolved PL spectra of Eu-doped ZnWO_4 precursors subjected to annealing at 400, 600, 800, and 1000 °C. The excitation wavelength is 375 nm and the detection wavelength is 480 nm. The raw data are represented by the circles, and the fitted curves are represented by the solid lines represent. It is found that each decay curve in Figure 18 can be fitted with one triple exponential function as described in Equation (7)

$$I(t) = A + B_1 \exp(-t/\tau_1) + B_2 \exp(-t/\tau_2) + B_3 \exp(-t/\tau_3) \quad (7)$$

where $I(t)$ stands for the PL intensity at time t , A is the baseline, B_i is the i th pre-exponential factor of the decay components, and τ_i is the i th decay time component ($i = 1-3$). The fitting parameters of the

time-resolved PL spectra are listed in Table 3. The parameter χ^2 in Table 3 represents the goodness of fit, and the average lifetime $\langle\tau\rangle$ is calculated by using the Equation (8) [41].

$$\langle\tau\rangle = (A_1\tau_1^2 + A_2\tau_2^2 + A_3\tau_3^2) / (A_1\tau_1 + A_2\tau_2 + A_3\tau_3) \quad (8)$$

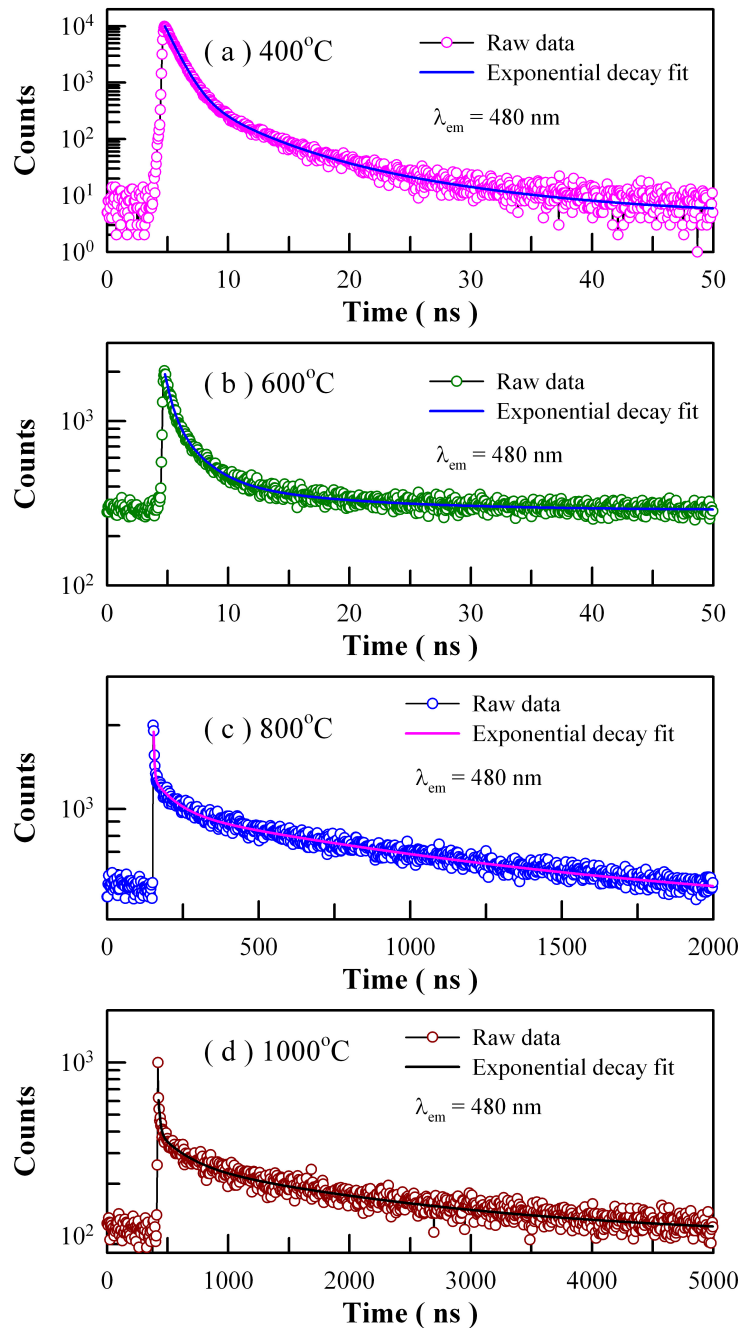


Figure 18. Time-resolved PL spectra of Eu-doped ZnWO₄ precursors subjected to annealing at different temperatures: (a) 400 °C; (b) 600 °C; (c) 800 °C; and (d) 1000 °C. The detection wavelength is fixed at 480 nm. The repetition frequencies of the pulsed diode laser are 20 MHz, 20 MHz, 500 kHz and 200 kHz, respectively.

Table 3. Fitting parameters of the time-resolved PL spectra of Eu-doped ZnWO₄ precursors subjected to annealing at different temperatures. The detection wavelength is 480 nm.

<i>T</i> (°C)	<i>A</i>	<i>B</i> ₁	<i>B</i> ₂	<i>B</i> ₃	τ_1 (ns)	τ_2 (ns)	τ_3 (ns)	τ (ns)	χ^2
400	4.560	9699.70	696.04	101.26	0.92	3.52	10.47	2.25	1.107
600	287.312	854.14	720.55	158.52	0.59	2.33	11.52	6.30	1.049
800	397.462	1227.99	316.41	575.56	2.85	78.00	1235.67	1191	0.976
1000	98.113	303.38	131.82	163.84	14.73	225.87	1939.88	1770	1.078

These parameters bear important information on the kinetics of carrier recombination. For example, the decay time constants are $\tau_1 = 0.92$ ns, $\tau_2 = 3.52$ ns and $\tau_3 = 10.47$ ns with $\langle \tau \rangle = 2.25$ ns for Eu-doped ZnWO₄ precursors subjected to annealing at 400 °C. It is noted that τ_1 is at the limit of the measurement capability of the instrument and therefore it merely represents the order of the short decay time constant [21,28,37,38]. The coexistence of τ_2 and τ_3 for each annealed sample suggests the presence of two different radiative recombination paths in ZnWO₄. Indeed, the two radiative recombination paths are determined in Figures 8 and 17. Alternatively, we have to note that the average PL lifetimes in Table 3 are particle size dependent. As can be seen in Table 3, the average lifetimes of first two samples (i.e., ZnWO₄ nanocrystals) are less than 10 ns whereas those of the last two samples (i.e., ZnWO₄ microcrystals) range from 1.19 μ s to 1.77 μ s. The average lifetime of ZnWO₄ microcrystals is about 100 times longer than that of ZnWO₄ nanocrystals, indicating the dramatic reduction in the non-radiative recombination paths in ZnWO₄ microcrystals. When compared to nanocrystals, ZnWO₄ microcrystals are characteristic of much less surface defects due to their reduced surface area. As is well known, these surface defects may act as PL quenching centers. Thus, the reduction in the surface defects is responsible for the prolonged average lifetimes of ZnWO₄ microcrystals.

The PL lifetimes of Eu emissions are usually longer than nanoseconds. In some cases, it can be extended into microseconds and even milliseconds. Figure 19 shows the time-resolved PL spectra of Eu-doped ZnWO₄ precursors subjected to annealing at 400, 600, 800, and 1000 °C. The excitation wavelength is 375 nm and the detection wavelength is 612 nm. Circles in Figure 19 represent the experiment data while the solid lines represent the fitted curves. It is found that each PL decay curve in Figure 19 can be fitted with one triple exponential function. The fitting parameters of the time-resolved PL spectra of Eu-doped ZnWO₄ phosphors are listed in Table 4. According to Equation (8), the average PL lifetimes of Eu³⁺ emissions at 612 nm are calculated to be 24.28, 5.20, 5.77 and 8.86 μ s for the Eu-doped ZnWO₄ precursors subjected to annealing at 400, 600, 800, and 1000 °C, respectively. As documented in the literature, Wang et al. reported that the average PL lifetime of Pr³⁺ doped ZnWO₄ at 607 nm was 5.40 μ s [41]. It is clear that the average PL lifetimes of Eu³⁺ emissions and Pr³⁺ emissions in ZnWO₄ are at the same order of magnitude. Since Eu is supposed to be located in a unique crystallographic site, namely Zn, we tried to fit each of the PL decay curves in Figure 19 with a unique exponential function. The decay time constants are derived to be 1.879, 1.548, 3.544, and 2.995 μ s for the samples annealed at 400, 600, 800, and 1000 °C, respectively. In the meanwhile, the values of goodness of fit are 1.536, 1.808, 2.617, and 2.208 for the samples annealed at 400, 600, 800, and 1000 °C, respectively. When compared to the fit with the sum of three exponential functions, the fit with a unique exponential function gives a much clearer picture of the underlying physical processes but suffers more from statistical reliability. It is obvious that much more work is needed in order to interpret the time-resolved PL spectra in Figure 19.

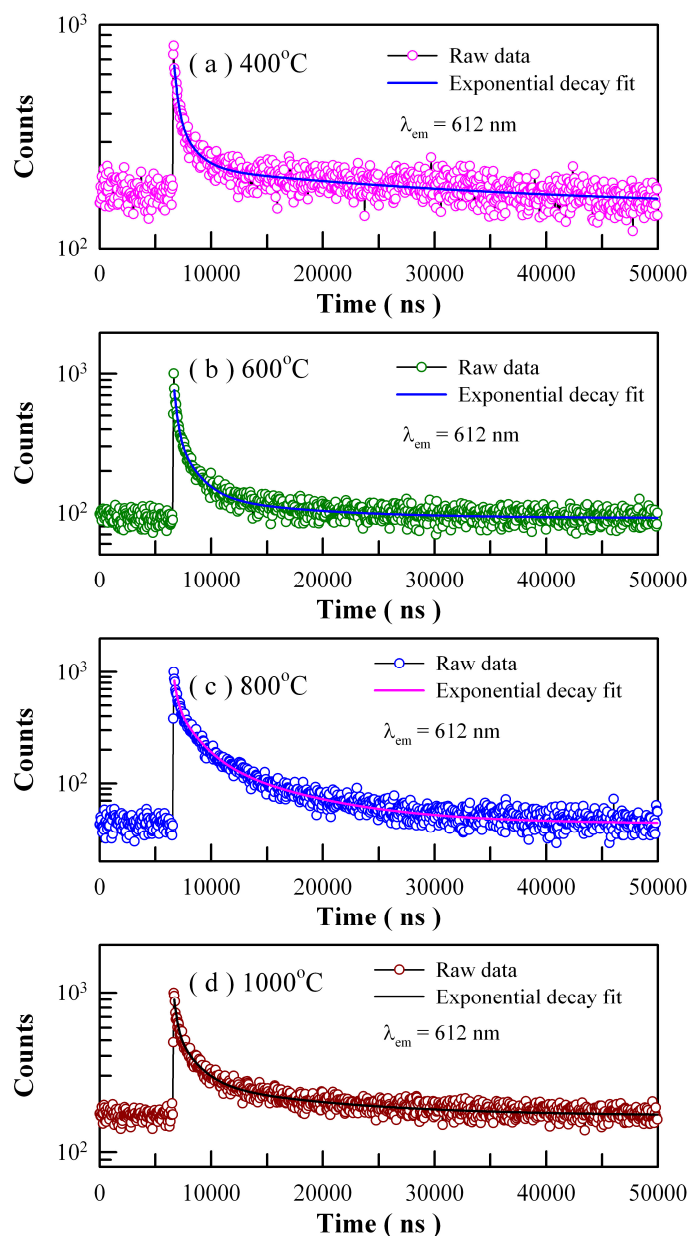


Figure 19. Time-resolved PL spectra of Eu-doped ZnWO₄ precursors subjected to annealing at different temperatures: (a) 400 °C; (b) 600 °C; (c) 800 °C; and (d) 1000 °C. The detection wavelength is fixed at 612 nm. The repetition frequency of the pulsed laser diode is 20 kHz.

Table 4. Fitting parameters of the time-resolved PL spectra of Eu-doped ZnWO₄ precursors subjected to annealing at different temperatures. The detection wavelength is 612 nm.

T (°C)	A	B_1	B_2	B_3	τ_1 (ns)	τ_2 (ns)	τ_3 (ns)	τ (μ s)	χ^2
400	150.000	289.91	181.83	81.17	330.28	1497.58	28,015	24.28	0.954
600	91.548	466.44	239.82	44.88	294.52	1639.56	9873	5.20	1.024
800	43.610	392.99	322.08	142.65	307.89	1841.62	8300	5.77	1.045
1000	168.249	381.88	312.29	107.85	280.61	1797.46	12491	8.86	1.144

4. Conclusions

Eu-doped ZnWO₄ phosphors were synthesized via the co-precipitation method followed by subsequent annealing at temperature in the range of 400–1000 °C. SEM characterizations show that

Eu-doped ZnWO₄ nanocrystals can grow into microcrystals as the annealing temperature increases from 400 to 1000 °C. It is found that the PL of Eu-doped ZnWO₄ is tunable through the control of the annealing temperature. By mixing the intrinsic defect emissions from ZnWO₄ host with the red emissions from extrinsic defects Eu³⁺ in the host, the luminescence color of Eu-doped ZnWO₄ can be adjusted in a controllable way, from purplish pink through greenish blue to white, through the control of annealing temperature. Density functional calculations and optical absorptions have confirmed that thermal annealing created intrinsic defects in ZnWO₄ lattices play a pivotal role in the color tunable emissions of the Eu³⁺ doped ZnWO₄ phosphors. Our results have demonstrated that intrinsic defect engineering in ZnWO₄ lattice is an alternative and effective strategy for tuning the emissions of Eu³⁺ doped ZnWO₄. This work shows how to harness the intrinsic defects in ZnWO₄ for the preparation of color tunable light-emitting phosphors, in which the emission tuning is uniquely positioned to adjust the intrinsic defects in ZnWO₄ lattice by the fine control of the annealing temperature. Under the framework of intrinsic defect engineering in host lattice, this strategy provides new capability of tuning the emissions from rare earth doped ZnWO₄ even when the rare earth doping concentration is fixed.

Author Contributions: Investigation, L.Y.; Writing-Original Draft Preparation, B.-g.Z.; Writing-Review & Editing, Y.M.H.

Funding: This research was funded by National Natural Science Foundation of China under grant numbers 11574036 and 11604028.

Acknowledgments: Xiazhang Li was acknowledged for the TEM characterizations.

Conflicts of Interest: The authors declare no conflict of interest.

References

1. Kraus, H.; Mikhailik, V.B.; Ramachers, Y.; Day, D.; Hutton, K.B.; Telfer, J. Feasibility study of a ZnWO₄ scintillator for exploiting materials signature in cryogenic WIMP dark matter searches. *Phys. Lett. B* **2005**, *610*, 37–44. [[CrossRef](#)]
2. Fu, H.; Lin, J.; Zhang, L.; Zhu, Y. Photocatalytic activities of a novel ZnWO₄ catalyst prepared by a hydrothermal process. *Appl. Catal. A Gen.* **2006**, *306*, 58–67. [[CrossRef](#)]
3. Yamaga, M.; Marshall, A.; O'Donnell, K.P.; Henderson, B. Polarized photoluminescence from Cr³⁺ ions in laser host crystals III. ZnWO₄. *J. Lumin.* **1990**, *47*, 65–70. [[CrossRef](#)]
4. Lou, Z.; Hao, J.; Cocivera, M. Luminescence of ZnWO₄ and CdWO₄ thin films prepared by spray pyrolysis. *J. Lumin.* **2002**, *99*, 349–354. [[CrossRef](#)]
5. Zhai, Y.Q.; Li, X.; Liu, J.; Jiang, M. A novel white-emitting phosphor ZnWO₄:Dy³⁺. *J. Rare Earths* **2015**, *33*, 350–354. [[CrossRef](#)]
6. He, H.Y. Preparation and luminescence property of Sm-doped ZnWO₄ powders and films with wet chemical methods. *Phys. Status Solidi B* **2009**, *246*, 177–182. [[CrossRef](#)]
7. Wen, F.S.; Zhao, X.; Huo, H.; Chen, J.S.; Shu-Lin, E.; Zhang, J.H. Hydrothermal synthesis and photoluminescent properties of ZnWO₄ and Eu³⁺-doped ZnWO₄. *Mater. Lett.* **2002**, *55*, 152–157. [[CrossRef](#)]
8. Chen, X.P.; Xiao, F.; Ye, S.; Huang, X.Y.; Dong, G.P.; Zhang, Q.Y. ZnWO₄:Eu³⁺ nanorods: A potential tunable white light-emitting phosphors. *J. Alloy. Compd.* **2011**, *509*, 1355–1359. [[CrossRef](#)]
9. Dong, T.T.; Li, Z.H.; Ding, Z.X.; Wu, L.; Wang, X.X.; Fu, X.Z. Characterizations and properties of Eu³⁺-doped ZnWO₄ prepared via a facile self-propagating combustion method. *Mater. Res. Bull.* **2008**, *43*, 1694–1701. [[CrossRef](#)]
10. Dai, Q.L.; Song, H.W.; Bai, X.; Pan, G.H.; Lu, S.Z.; Wang, T.; Ren, X.G.; Zhao, H.F. Photoluminescence properties of ZnWO₄:Eu³⁺ nanocrystals prepared by a hydrothermal method. *J. Phys. Chem. C* **2007**, *111*, 7586–7592. [[CrossRef](#)]
11. Yan, B.; Lei, F. Molten salt synthesis, characterization and luminescence of ZnWO₄:Eu³⁺ nanophosphors. *J. Alloy Compd.* **2010**, *507*, 460–464. [[CrossRef](#)]
12. Li, C.Y.; Du, X.D.; Yue, D.; Wang, M.N.; Huang, J.B.; Wang, Z.L. Color changing from white to red emission for ZnWO₄:Eu³⁺ nanophosphors at different temperature. *Mater. Lett.* **2016**, *171*, 27–29. [[CrossRef](#)]

13. Li, C.Y.; Du, X.D.; Yue, D.; Gao, J.N.; Wang, Z.L. Full-color emission based ZnWO₄ spherical nanoparticles through doping of rare earth ions. *Mater. Lett.* **2013**, *108*, 257–260. [[CrossRef](#)]
14. Zhou, Y.; Xu, J.Y.; Zhang, Z.J.; You, M.J. The spectroscopic properties of Dy³⁺ and Eu³⁺ co-doped ZnWO₄ phosphors. *J. Alloy Compd.* **2014**, *615*, 624–628. [[CrossRef](#)]
15. Zhai, Y.Q.; Wang, M.; Zhao, Q.; Yu, J.B.; Li, X.M. Fabrication and luminescent properties of ZnWO₄:Eu³⁺, Dy³⁺ white light-emitting phosphors. *J. Lumin.* **2016**, *172*, 161–167. [[CrossRef](#)]
16. Guo, X.; Sun, Z.; Sietsma, J.; Yang, Y. Semiempirical model for the solubility of rare earth oxides in molten fluorides. *Ind. Eng. Chem. Res.* **2016**, *55*, 4773–4781. [[CrossRef](#)]
17. Zhu, X.; Sun, S.; Liu, C.; Tu, G. Solubility of Re₂O₃ (Re = La and Nd) in light rare earth fluoride molten salts. *J. Rare Earths* **2018**, *36*, 765–771. [[CrossRef](#)]
18. Zhang, S.; Hao, Z.; Zhang, L.; Pan, G.H.; Wu, H.; Zhang, X.; Luo, Y.; Zhang, L.; Zhao, H.; Zhang, J. Efficient blue-emitting phosphor SrLu₂O₄:Ce³⁺ with high thermal stability for near ultraviolet (~400 nm) LED-chip based white LEDs. *Sci. Rep.* **2018**, *8*, 10463. [[CrossRef](#)]
19. Honmaa, T.; Toda, K.; Ye, Z.G.; Sato, M. Concentration quenching of the Eu³⁺-activated luminescence in some layered perovskites with two-dimensional arrangement. *J. Phys. Chem. Solids* **1998**, *59*, 1187–1193. [[CrossRef](#)]
20. Han, B.; Zhang, J.; Wang, Z.; Liu, Y.; Shi, H. Investigation on the concentration quenching and energy transfer of red-light-emitting phosphor Y₂MoO₆:Eu³⁺. *J. Lumin.* **2014**, *149*, 150–154. [[CrossRef](#)]
21. Huang, Y.M.; Li, M.Y.; Yang, L.; Zhai, B.G. Eu²⁺ and Eu³⁺ doubly doped ZnWO₄ nanoplates with superior photocatalytic performance for dye degradation. *Nanomaterials* **2018**, *8*, 765. [[CrossRef](#)] [[PubMed](#)]
22. Zhai, B.G.; Liu, D.; He, Y.; Yang, L.; Huang, Y.M. Tuning the photoluminescence of Eu²⁺ and Eu³⁺ co-doped SrSO₄ through post annealing technique. *J. Lumin.* **2018**, *194*, 485–493. [[CrossRef](#)]
23. Perdew, J.P.; Burke, K.; Ernzerhof, M. Generalized gradient approximation made simple. *Phys. Rev. Lett.* **1996**, *77*, 3865–3868. [[CrossRef](#)] [[PubMed](#)]
24. Zhai, B.G.; Yang, L.; Ma, Q.L.; Liu, X.; Huang, Y.M. Mechanism of the prolongation of the green afterglow of SrAl₂O₄:Dy³⁺ caused by the use of H₃BO₃ flux. *J. Lumin.* **2017**, *181*, 78–87. [[CrossRef](#)]
25. Su, Y.; Zhu, B.; Guan, K.; Gao, S.; Lv, L.; Du, C.; Peng, L.; Hou, L.; Wang, X. Particle size and structural control of ZnWO₄ nanocrystals via Sn²⁺ doping for tunable optical and visible photocatalytic properties. *J. Phys. Chem. C* **2012**, *116*, 18508–18517. [[CrossRef](#)]
26. Bøjesen, E.D.; Jensen, K.M.Ø.; Tyrsted, C.; Mamakhel, A.; Andersen, H.L.; Reardon, H.; Chevalier, J.; Dippele, A.C.; Iversen, B.B. The chemistry of ZnWO₄ nanoparticle formation. *Chem. Sci.* **2016**, *7*, 6394–6406. [[CrossRef](#)] [[PubMed](#)]
27. Shannon, R.D. Revised effective ionic radii and systematic studies of interatomic distances in halides and chalcogenides. *Acta Cryst.* **1976**, *32A*, 751–767. [[CrossRef](#)]
28. Zhai, B.G.; Ma, Q.L.; Yang, L.; Huang, Y.M. Synthesis and optical properties of Tb-doped pentazine dimolybdate pentahydrate. *Results Phys.* **2017**, *7*, 3991–4000. [[CrossRef](#)]
29. Zhai, B.G.; Ma, Q.L.; Yang, L.; Huang, Y.M. Effects of sintering temperature on the morphology and photoluminescence of Eu³⁺ doped zinc molybdenum oxide hydrate. *J. Nanomater.* **2018**, *2018*, 7418508. [[CrossRef](#)]
30. Huang, Y.M.; Ma, Q.L.; Zhai, B.G. Wavelength tunable photoluminescence of ZnO/porous Si nanocomposites. *J. Lumin.* **2013**, *138*, 157–163. [[CrossRef](#)]
31. Schneider, W.D.; Laubschat, C.; Nowik, I.; Kaindl, G. Shake-up excitations and core-hole screening in Eu systems. *Phys. Rev. B* **1981**, *24*, 5422–5425. [[CrossRef](#)]
32. Han, M.; Oh, S.; Park, J.H.; Park, H.L. X-ray photoelectron spectroscopy study of CaS:Eu and SrS:Eu phosphors. *J. Appl. Phys.* **1993**, *73*, 4546–4549. [[CrossRef](#)]
33. Zhai, B.G.; Ma, Q.L.; Xiong, R.; Liu, X.; Huang, Y.M. Blue-green afterglow of BaAl₂O₄:Dy³⁺ phosphors. *Mater. Res. Bull.* **2016**, *75*, 1–6. [[CrossRef](#)]
34. Ma, Q.L.; Xiong, R.; Huang, Y.M. Tunable photoluminescence of porous silicon by liquid crystal infiltration. *J. Lumin.* **2011**, *131*, 2053–2057. [[CrossRef](#)]
35. Gritsenko, V.A.; Islamov, D.R.; Perevalov, T.V.; Aliev, V.S.; Yelisseyev, A.P.; Lomonova, E.E.; Pustovarov, V.A.; Chin, A. Oxygen vacancy in hafnia as a blue luminescence center and a trap of charge carriers. *J. Phys. Chem. C* **2016**, *120*, 19980–19986. [[CrossRef](#)]

36. Zhai, B.G.; Huang, Y.M. Green photoluminescence and afterglow of Tb doped SrAl₂O₄. *J. Mater. Sci.* **2017**, *52*, 1813–1822. [[CrossRef](#)]
37. Huang, Y.M.; Ma, Q.L. Long afterglow of trivalent dysprosium doped strontium aluminate. *J. Lumin.* **2015**, *160*, 271–275. [[CrossRef](#)]
38. Zhai, B.G.; Yang, L.; Ma, Q.L.; Huang, Y.M. Growth of ZnMoO₄ nanowires via vapor deposition in air. *Mater. Lett.* **2017**, *188*, 119–122. [[CrossRef](#)]
39. Kalinko, A.; Kuzmin, A.; Evarestov, R.A. Ab initio study of the electronic and atomic structure of the wolframite-type ZnWO₄. *Solid State Commun.* **2009**, *149*, 425–428. [[CrossRef](#)]
40. Zhao, X.; Yao, W.; Wu, Y.; Zhang, S.; Yang, H.; Zhu, Y. Fabrication and photoelectrochemical properties of porous ZnWO₄ film. *J. Solid State Chem.* **2006**, *179*, 2562–2570. [[CrossRef](#)]
41. Wang, K.; Feng, W.; Feng, X.; Li, Y.; Mi, P.; Shi, S. Synthesis and photoluminescence of novel red-emitting ZnWO₄:Pr³⁺, Li⁺ phosphors. *Spectrochim. Acta A* **2016**, *154*, 72–75. [[CrossRef](#)]



© 2019 by the authors. Licensee MDPI, Basel, Switzerland. This article is an open access article distributed under the terms and conditions of the Creative Commons Attribution (CC BY) license (<http://creativecommons.org/licenses/by/4.0/>).